



1 **Modulation of the seasonal cycle of the Antarctic sea ice extent by sea ice**
2 **processes and feedbacks with the ocean and the atmosphere**

3

4 Hugues Goosse¹, Sofia Allende Contador¹, Cecilia M. Bitz², Edward Blanchard-Wrigglesworth², Clare
5 Eayrs³, Thierry Fichefet¹, Kenza Himmich⁴, Pierre-Vincent Huot⁵, François Klein¹, Sylvain Marchi⁵,
6 François Massonnet¹, Bianca Mezzina¹, Charles Pelletier⁶, Lettie Roach^{7,8}, Martin Vancoppenolle⁴,
7 Nicole P.M. van Lipzig⁵

- 8 1. Earth and Life Institute, Université catholique de Louvain, Belgium
9 2. Department of Atmospheric Sciences, University of Washington, Seattle, USA
10 3. Center for global Sea Level Change, New York University Abu Dhabi, United Arab Emirates
11 4. Sorbonne Université, Laboratoire d'Océanographie et du Climat (LOCEAN-IPSL), CNRS, IRD,
12 MNHN, Paris, France
13 5. Department of Earth and Environmental Sciences, KU Leuven, Leuven, Belgium
14 6. European Centre for Medium-Range Weather Forecasts, Bonn, Germany
15 7. NASA Goddard Institute for Space Studies, New York, NY, USA
16 8. Center for Climate Systems Research, Columbia University, New York, NY, USA

17
18
19

20 Corresponding author: Hugues Goosse hugues.goosse@uclouvain.be

21
22
23



24 **Abstract**

25 The seasonal cycle of the Antarctic sea ice extent is strongly asymmetric, with a relatively slow increase
26 after the summer minimum followed by a more rapid decrease after the winter maximum. This cycle
27 is intimately linked to the seasonal cycle of the insolation received at the top of the atmosphere but
28 sea ice processes as well as the exchanges with the atmosphere and ocean may also play a role. To
29 quantify these contributions, a series of idealized sensitivity experiments have been performed with
30 an eddy-permitting (1/4°) NEMO-LIM3 Southern Ocean configuration including a representation of ice
31 shelf cavities, in which the model was either driven by an atmospheric reanalysis or coupled to the
32 COSMO-CLM² regional atmospheric model. In those experiments, sea ice thermodynamics and
33 dynamics as well as the exchanges with the ocean and atmosphere are strongly perturbed. This is
34 achieved by modifying snow and ice thermal conductivities, the vertical mixing in the ocean top layers,
35 the effect of freshwater uptake/release upon sea ice growth/melt, ice dynamics and surface albedo.
36 We find that the evolution of sea ice extent during the ice advance season is largely independent of
37 the direct effect of the perturbation and appears thus mainly controlled by initial state in summer and
38 subsequent insolation changes. In contrast, the melting rate varies strongly between the experiments
39 during the retreat, in particular if the surface albedo or sea ice transport are modified, demonstrating
40 a strong contribution of those elements to the evolution of ice coverage through spring and summer.
41 As with the advance phase, the retreat is also influenced by conditions at the beginning of the melt
42 season in September. Atmospheric feedbacks enhance the model winter ice extent response to any of
43 the perturbed processes, and the enhancement is strongest when the albedo is modified. The response
44 of sea ice volume and extent to changes in entrainment of subsurface warm waters to the ocean
45 surface is also greatly amplified by the coupling with the atmosphere.

46 **Short Summary** (500 characters)

47 Using idealized sensitivity experiments with a regional atmosphere-ocean-sea ice model, we show that
48 the sea ice advance is constrained by initial conditions in March while the retreat season is influenced
49 by the magnitude of several physical processes, in particular by the ice-albedo feedback and ice
50 transport. Atmospheric feedbacks amplify the response of the winter ice extent to perturbations while
51 some negative feedbacks related to heat conduction fluxes act on the ice volume.

52



53 **1. Introduction**

54 The sea ice extent in the Southern Ocean, defined as the ocean surface covered by at least 15% of
55 sea ice, displays a very pronounced seasonal cycle with a minimum in February of about 3 million km²
56 and a maximum in September of more than 18 million km² on average over the last decades (Parkinson,
57 2014, 2019; Handcock and Raphael, 2020) (Fig. 1). In contrast to the Arctic, where multiyear ice
58 accounted for a significant fraction of the total ice extent -at least until the end of the 20th century-,
59 the Antarctic sea ice cover is mainly seasonal, with sea ice only present in summer in some regions
60 close to the coast, in particular in the Weddell and Ross Seas.

61 The seasonal cycle of Antarctic sea ice extent is highly asymmetric, with a minimum around Julian
62 day 50 (February 19) and a maximum on average close to day 260 (September 18) (Stammerjohn et
63 al., 2008; Massom et al., 2013; Handcock and Raphael, 2020; Raphael et al., 2020; Roach et al., 2022).
64 The advance season, defined as the time between the minimum and maximum ice extents, is thus
65 about two months longer than the retreat season, defined as the time from maximum to minimum.

66 It has been suggested that this asymmetry is related to the variations of the mean position of the
67 westerly winds that blow over the Southern Ocean associated with the Semi Annual Oscillation (SAO)
68 (Enomoto and Ohmura, 1990; Watkins and Simmonds, 1999; Eayrs et al., 2019). This mode of variability
69 of the Antarctic climate induces a larger divergence of the sea ice pack in spring and thus a rapid
70 melting, while the divergence is weaker in autumn, leading to a slower expansion of the pack. A
71 complementary mechanism explaining the rapid seasonal retreat of the sea ice is the positive ice-
72 albedo feedback, in which a decrease in ice concentration yields a larger absorption of solar radiation
73 and enhances the ice melting (Gordon, 1981; Nihashi and Cavalieri, 2006). A possible role of the
74 oceanic heat input has also been proposed (Gordon, 1981). However, the vertical ocean heat transport
75 from the relatively warm ocean below the mixed layer to the surface is higher in autumn and winter
76 when the stratification is weak than in spring and summer when it is strong (Gordon, 1981; Martinson,
77 1990). The seasonality of the vertical oceanic transport alone could thus not explain the asymmetry in
78 the seasonal cycle of the sea ice extent (Eayrs et al., 2019), but it could have an indirect effect, for
79 instance through its effect on the ice thickness (Martinson, 1990; Goosse et al., 2018; Wilson et al.,
80 2019).

81 Nevertheless, a recent study based on idealized climate models has demonstrated that the
82 asymmetry of the seasonal cycle of the ice extent is due to the seasonal cycle of incoming solar
83 radiation (Roach et al., 2022). The period with relatively high incoming solar radiation in spring and
84 summer induces a rapid melting season and a fast retreat of the sea ice, while a long period with low
85 insolation in autumn and winter favors a longer growing season. This relatively direct mechanism is
86 very robust and explains why the asymmetry is observed each year and is reproduced by a wide range
87 of models, from very simple ones to the most complex Earth System models (Eayrs et al., 2019; Roach
88 et al., 2022).

89 Identifying the seasonal cycle of insolation as the main contributor to the asymmetry of the
90 seasonal cycle of the Antarctic sea ice extent is a major achievement. However, the atmosphere, sea
91 ice and ocean dynamics still play a role and may modulate the magnitude of the asymmetry.
92 Furthermore, the seasonal cycle of the sea ice extent is characterized by many other elements in
93 addition to this asymmetry, such as its amplitude or the timing of the maximum retreat. Factors
94 controlling those characteristics also need to be analyzed to quantify how the seasonal cycle of the
95 Antarctic sea ice influences the dynamics of the climate at high southern latitudes. Models still have
96 large biases on those aspects and a better understanding is necessary for model improvement (Downes
97 et al., 2015; Eayrs et al., 2019; Roach et al., 2020; Raphael et al., 2020; Schroeter and Sandery, 2022).



98 Several studies have addressed the role of sea ice processes and atmosphere and ocean feedbacks
99 on Antarctic sea ice extent, focusing both on the mean seasonal cycle and the interannual variability
100 (e.g., Fichfet and Morales Maqueda, 1997; Holland and Kimura, 2016; Hobbs et al., 2016; Kushara et
101 al., 2019). An instructive diagnostic is to decompose the contribution of the dynamics, including the
102 transport of sea ice, from the one of thermodynamics that influences the local formation or melting of
103 sea ice. This decomposition is not always straightforward, as for example winds control both the sea
104 ice transport and the advection of warm or cold air masses that impacts thermodynamic processes.
105 The results may also depend on the definition of the dynamics and thermodynamics contributions.
106 Nevertheless, a common conclusion is that the thermodynamic processes play a strong role nearly all
107 year long, with a clearly dominant contribution during the advance period, while the impact of the
108 winds becomes more important later in the season, in particular during the retreat (Fichfet and
109 Morales Maqueda, 1997; Holland and Kimura, 2016; Kushara et al., 2019; Eayrs et al., 2020).

110 Despite those advances, many uncertainties remain around the processes controlling the seasonal
111 cycle of the Antarctic sea ice, in particular because the majority of existing studies address only some
112 of the processes, forbidding a comparison between different factors, or are devoted to the variability
113 and trends, not to the seasonal cycle itself. As a consequence, our goal here is to propose an analysis
114 of the different processes in a single framework, using sensitivity experiments designed to the study
115 of the seasonal cycle. Specifically, we perform sensitivity experiments with a sea-ice-ocean model
116 driven by an atmospheric reanalysis and the same model coupled to a regional atmospheric model,
117 disabling or strongly perturbing key processes related to sea ice dynamics and thermodynamics as well
118 as the exchanges between the atmosphere and ocean.

119 The goal of those sensitivity experiments is not to impose realistic changes or to improve
120 agreement with observations but rather to determine the role of the associated processes. In contrast
121 to many existing sensitivity studies performed with sea ice-ocean models, the experiments with the
122 coupled model will address the limitations associated with a prescribed atmospheric state, which tends
123 to damp the changes imposed by the perturbation as the location of the sea ice edge is strongly
124 controlled by the atmospheric forcing, in particular in winter (e.g., Urrego-Blanco et al, 2016).
125 Furthermore, the comparison between the experiments with and without coupling with the
126 atmosphere will, for the first time, quantify the regional atmospheric feedbacks in response to the
127 imposed perturbation. The sensitivity experiments last only two years and are not analyzed at
128 equilibrium for two reasons. First, the drift of the model state after several years in response to the
129 perturbation can be large. The relative importance of the various processes, which may depend of the
130 mean state, can thus be very different from the one in the current climate. Second, by comparing the
131 first years of each experiment, which start with identical conditions at the beginning of the season,
132 and the second year, for which the perturbation has already acted during one year, we can determine
133 the contribution of the initial state and the one of the processes occurring during the sea ice advance
134 and retreat seasons. This approach is also instructive for understanding observed changes and for
135 predictions as this distinction between initial conditions and ongoing perturbations is key in
136 interpreting the observed variability. Many studies have demonstrated that large spatial variations are
137 present between the different sectors of the Southern Ocean (e.g., Parkinson et al., 2019; Kushara et
138 al., 2019; Kacimi and Kwok, 2020). Analyzing them is necessary to have a full picture of the dynamics
139 of the system. Nevertheless, we will focus here first on the ice extent integrated over the whole
140 Southern Ocean, keeping the regional changes for future work except when critically needed to
141 interpret the integrated changes. The models used and the perturbation applied are described in
142 Section 2. Section 3 presents the main results of the sensitivity experiments. Section 4 is devoted to
143 the atmospheric feedbacks. Section 5 includes a discussion and a synthesis of our main results.



144

145 **2 Methodology**

146 Model description

147 The simulations are performed with a regional circum-Antarctic configuration of the sea-ice-ocean
148 model NEMO-LIM3 version 3.6 (Rousset et al., 2015) driven by the ERA5 atmospheric reanalysis
149 (Hersbach et al., 2020) and with NEMO-LIM3 coupled to the COSMO-CLM² regional atmospheric model
150 (Pelletier et al., 2022a). The model set-up and forcing are identical to Verfaillie et al. (2022) for NEMO-
151 LIM3 driven by ERA5 and to Pelletier et al. (2022a) for NEMO-LIM-COSMO-CLM², except that, for the
152 latter, a bug in the interpolation of the winds in the coupling between the ocean and atmosphere has
153 been corrected (Pelletier et al., 2022b). The version of NEMO-LIM3 driven by ERA5 will hereafter be
154 referred to NEMO and the version coupled to COSMO-CLM² as PARASO following Pelletier et al.
155 (2022a).

156 NEMO (Nucleus for European Modelling of the Ocean, Madec et al., 2017) includes the OPA ocean
157 model (Océan PARallélisé) coupled with the Louvain-la-Neuve sea ice model (Vancoppenolle et al.,
158 2012; Rousset et al., 2015). Our configuration has an explicit representation of Antarctic ice shelf
159 cavities using the implementation of Mathiot et al. (2017). The free-surface oceanic component is
160 hydrostatic and applies finite differences to solve the equations on an Arakawa C-grid. Vertical mixing
161 is computed using a turbulent kinetic energy (TKE) scheme (Gaspar et al., 1990), while lateral diffusion
162 of momentum is carried out with a bi-Laplacian viscosity and isopycnal diffusion of tracers with a
163 Laplacian operator. Oceanic convection is represented using an enhanced vertical diffusivity, triggered
164 under unstable vertical stratification (Lazar et al., 1999). The sea ice component uses an elastic-viscous-
165 plastic rheology (Bouillon et al., 2013) and a five-category ice-thickness distribution (Bitz et al., 2001;
166 Massonnet et al., 2019). Each of those categories is covered by snow, with one snow thickness per
167 category. The energy conserving sea ice thermodynamics follows Bitz and Lipscomb (1999) and
168 includes an explicit representation of the evolution of salt content and its impact on the sea ice
169 properties (Vancoppenolle et al., 2009). The albedo of sea ice depends on snow and ice thickness,
170 surface temperature and cloud cover (Grenfell and Perovich, 2004; Brandt et al., 2005).

171 The model grid is ePERIANT025 (Mathiot et al., 2017) that has a nominal horizontal resolution of $\frac{1}{4}$
172 of a degree with an isotropic spacing, meaning that the resolution is about 24 km at 30°S but increases
173 up to 3.8 km over the Antarctic continental shelf. A z-coordinate is applied on the vertical using 75
174 levels, with a thickness of about 1m at surface reaching 200m at depth and partial steps in the bottom
175 layer (and in the top layer beneath ice shelves). In the uncoupled simulations, NEMO is driven at the
176 surface by the fluxes computed by the CORE bulk formulas (Large et al., 2004) using 3-hourly fields
177 derived from the ERA5 reanalysis (Hersbach et al., 2020). The conditions at the northern boundary of
178 the domain (30°S) are prescribed from the ORAS5 ocean reanalysis (Zuo et al., 2019).

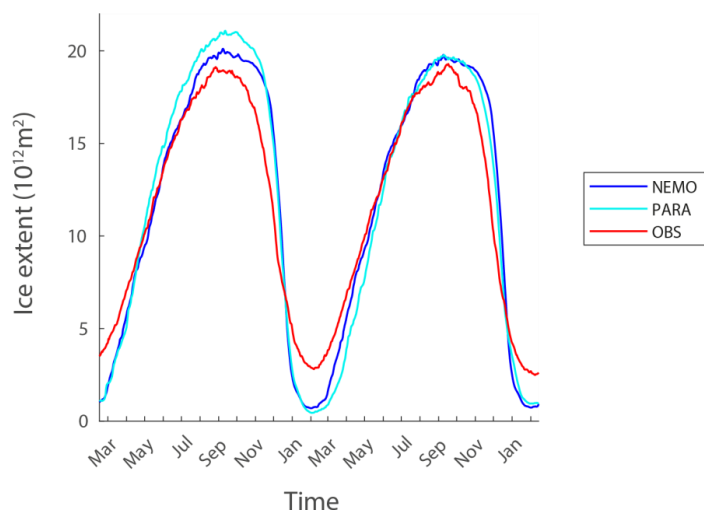
179 In PARASO, NEMO is coupled to COSMO-CLM², which includes the version 5.0 of the Consortium
180 for Small-scale MOdeling (COSMO) regional atmospheric model (Rockel et al., 2008) and the
181 Community Land Model version 4.5 (Oleson et al., 2013). COSMO is a non-hydrostatic model using
182 generalized terrain-following height coordinates with 60 levels (Doms and Baldauf, 2018). The version
183 utilized here includes parameter calibration adapted to polar regions and a new snow scheme
184 (Souverein et al., 2018). Furthermore, the computation of the fluxes is separated over land, ocean and
185 sea ice surfaces for the coupling with NEMO (Pelletier et al., 2022a). The conditions at the lateral
186 boundary of the domain are obtained from ERA5. COSMO-CLM² uses a rotated latitude-longitude grid
187 with a horizontal resolution of 0.22°, which corresponds to about 25 km. The domain is smaller than



188 the one of NEMO, with a northern boundary located between 50°S and 40°S. In the areas not simulated
189 by COSMO-CLM², NEMO is forced by ERA5 fields as in the uncoupled configuration.

190 Experimental design

191 NEMO is driven by the ERA5 reanalysis using every year the forcing from the period 1st May 1990
192 to 30th April 1991, which is considered a normal period regarding the major modes of climate
193 variability (Stewart et al., 2020; Verfaillie et al., 2022). This simulation thus has no interannual
194 variability in order to focus specifically on the seasonal cycle, while keeping conditions close to the
195 model climatology. The two-year simulations analyzed here follow a 10-year spin-up, which is sufficient
196 to have a quasi-equilibrium for the surface variables (Verfaillie et al., 2022). The PARASO simulation
197 has been initialized in 1985 and we discuss here two-year simulations following a 10-year spinup,
198 meaning that the analyses start in 1995. The conditions are thus slightly different in the two
199 configurations. Nevertheless, the mean states of the coupled and uncoupled models are also different,
200 forbidding a direct comparison between them anyway (Fig. 1). Both configurations underestimate the
201 sea ice extent in summer, and tend to overestimate it in winter. They also have a delayed and too rapid
202 retreat season. Those biases are similar to those found in many other coupled and uncoupled models
203 (Downes et al., 2015; Eayrs et al., 2019; Roach et al., 2020; Raphael et al., 2020; Schroeter and Sandery,
204 2022). Each sensitivity experiment will be compared to the reference simulation using the same model
205 configuration and initial state, assuming that the biases are small enough to have only a marginal effect
206 on the response to the perturbation. Additionally, in contrast to NEMO alone, PARASO can develop
207 some internal variability despite the strong constraints at its boundaries. Ideally, an ensemble of
208 simulations should be performed for each of the coupled experiments, but this exceeds available
209 computing capacities. Tests with identical configurations but slight perturbations of the initial state
210 indicate that the difference in ice extent is usually much smaller than 0.2 million km², i.e. less than the
211 response to the perturbation in the majority of the experiments, but the possibility that some of the
212 differences between the experiments are just occurring by chance must be kept in mind.



213

214 Figure 1. Seasonal cycle of the Antarctic sea ice extent (in 10¹² m²) in observations (Fetterer et al.,
215 2017) and in the reference experiments with NEMO and PARASO (starting in March). For observations and PARASO,
216 the period from March 1995 to February 1997 is shown while for NEMO the forcing
217 corresponds to the 'normal period' from May 1990 to April 1991 that is applied twice.



218 Set-up of the sensitivity experiments

219 Identical perturbations are applied in NEMO and PARASO on the 1st of March and 1st of September
220 in the 2-year sensitivity experiments (see Table 1). The first two experiments are devoted to the role
221 of the exchanges between sea ice and the oceanic mixed layer. In the first one (Mix100), the ocean
222 temperatures and salinities are homogenized from the surface to 100m depth at each time step by
223 completely mixing the corresponding grid boxes in each column. This depth roughly corresponds to
224 the seasonal maximum depth of the mixed layer in the model in most ice-covered regions except over
225 the continental shelf (e.g., Barthélemy et al., 2015). The effect of this mixing scheme perturbation is
226 that the seasonal summer shoaling of the mixed layer due to freshening is removed. The goal is to
227 determine whether such deep summer mixing favors heat storage at the surface and delays the sea
228 ice advance. In the second experiment (NoMassFlux), sea ice growth and melt is no longer associated
229 with freshwater uptake and release. This is equivalent to assuming that sea ice salinity is the same as
230 the ocean surface salinity. Therefore, the surface ocean salinity no longer responds to sea ice formation
231 and melting. This disables the negative ice production-entrainment feedback (Martinson, 1990) in
232 which the upper ocean salinity increase due to ice formation induces a mixed layer deepening and
233 entrainment of deeper warmer water towards the surface that reduces ice formation. The absence of
234 this negative feedback in NoMassFlux could thus potentially accelerate the sea ice advance.

235 The second group of experiments is devoted to sea ice physics and properties. As sea ice thickness
236 is a key characteristic of the pack that strongly controls its behavior, the first two experiments
237 artificially increase (ThickIce) and decrease (ThinIce) the ice thickness. This is achieved by increasing
238 (ThickIce) and decreasing (ThinIce) the thermal conductivities of the ice and snow by a factor of five.
239 With low conductivity, ice becomes a much better insulator for the ocean that loses less heat to the
240 atmosphere in fall and winter, inducing a slower increase in ice thickness. We expect then that a
241 thinner ice will melt faster in spring, accelerating the ice retreat. As the ice-albedo feedback is expected
242 to be a dominant element of the seasonal sea ice retreat, setting both the albedo of the snow and ice
243 to the ocean value in AlbOce should accelerate the retreat.

244 We also test the impact of ice dynamics by disabling it (NoIceDyn). The ice dynamics are expected
245 to favor a faster sea ice advance in fall by transporting sea ice from the colder regions, where it is
246 quickly replaced because of strong ice formation, to the north where it can survive because of the
247 relatively low temperature. It also accelerates the retreat in spring by transferring sea ice to regions
248 where it is warm enough during this season to quickly melt and by creating leads within the pack that
249 enhances the ice-albedo feedback. Suppressing ice dynamics should thus reduce the amplitude of the
250 seasonal cycle of the sea ice extent. For technical reasons, the implementation of sea-ice dynamics
251 suppression differs in uncoupled and coupled experiments: in the former, all the sea-ice dynamic
252 components of the model are disabled; in the latter, solely the velocity and large-scale transport is set
253 to zero in PARASO (other mechanisms such as ridging are active).

254 Although no sensitivity experiment includes explicit modifications of atmospheric parameters or
255 processes, all of the applied perturbations affect indirectly the exchanges between the ocean-sea-ice
256 system and the atmosphere by modifying the surface conditions. Comparing the coupled and
257 uncoupled configurations quantifies the contribution of the atmospheric feedbacks.

258

259

260



261 Table 1. List of experiments. Each experiment is performed for 2 years with NEMO and PARASO
262 and for two starting dates, March 1 and September 1. For references in the text, NEMO and PARASO
263 experiments have the additional suffixes NEMO and PARA, respectively, while for the two starting
264 dates we use the suffixes Mar and Sep.

Short name	Description
Ref	Reference experiment without perturbation
Mix100	Ocean mixed over the top 100m of the ocean all year long
NoMassFlux	No mass flux associated with the sea ice formation or melting
ThickIce	Sea ice and snow thermal conductivities divided by 5
ThinIce	Sea ice and snow thermal conductivities multiplied by 5
AlbOce	Sea ice and snow albedos equal to that of the ocean (=0.088)
NolceDyn	Ice dynamics disabled (uncoupled mode); or sea ice velocity equals zero (coupled mode).

265

266 3 Results

267 *First advance season*

268 In the sensitivity experiments starting in March, the perturbations applied to the model physics
269 have very little impact on the sea ice advance until August (Fig. 2ab), both in the coupled and
270 uncoupled model configurations. When starting from identical initial conditions, the sea ice advance
271 seems thus controlled by external conditions imposed by the seasonal evolution of the insolation and
272 does not depend much on the sea ice physics or on the interactions between sea ice, the ocean and
273 the atmosphere. Even the absence of sea ice transport (experiment NolceDyn_NEMO_Mar and
274 NolceDyn_PARA_Mar) has nearly no effect on the total sea ice extent during this period, confirming
275 previous studies indicating that the sea advance is mainly of thermodynamic nature (e.g., Fichefet and
276 Morales Maqueda, 1997; Kusahara et al., 2019). The impact on the sea ice volume is more immediate,
277 with a difference that can reach more than a factor two in August between some experiments such as
278 ThickIce_NEMO_Mar and Thin_NEMO_Mar (Fig. 3a). Nevertheless, this change in volume has little
279 impact on the extent, showing a decoupling between the two variables in our experiments during this
280 first advance season.

281 The different experiments have varying ice growth rates, consistent with the differences in ice
282 volume, but the temporal evolution is relatively similar during the advance season (Fig. 4). ThickIce
283 and NoMassflux stand as exceptions. In ThickIce, the ice production-entrainment feedback is very
284 active as a consequence of the large sea ice formation and brine release that destabilizes the water
285 column. The oceanic mixed layer depth (Fig. S1) is thus much larger than in the other experiments and
286 the associated vertical ocean-to-ice sensible heat transfer compensates early in the season for a
287 significant fraction of the cooling imposed at surface, explaining the early peak in the freezing rate (for
288 instance the peak occurs in day 166 in ThickIce_NEMO_Mar compared to day 220 in the corresponding
289 reference simulation). In NoMassFlux, by contrast, as the ice production-entrainment feedback is
290 inactive by design, the oceanic mixing is much weaker and strong ice formation can be sustained until
291 the end of the growth season, particularly in the PARASO configuration, with a peak in ice formation
292 in NoMassFlux_PARA_Mar on day 247 compared to day 187 in the corresponding reference simulation.

293 *Maximum extent and retreat season*

294 The modification of the ice volume imposed by the perturbations has only a weak impact on the
295 sea ice extent until August, as indicated above, but experiments with thicker ice tend to have a larger



296 sea ice extent after August, a longer plateau with an extent close to the maximum, and a slower retreat.
297 For instance, ThickIce_NEMO_Mar, which has the largest volume for all the experiments with NEMO,
298 has a maximum ice extent that is higher than in Thin_NEMO_Mar by 1.2 million km², a delayed
299 beginning of the retreat in this experiment, and an extent that is larger than in Thin_NEMO_Mar by
300 3.3 million km² at the end of November (Fig. 2a). The impact of volume differences on the date of the
301 maximum extent itself is generally weak (see Tables 2 and 3), but a link between the maximum volume
302 and the date at which the sea ice extent decreases to 95% of its maximum is clear in most experiments
303 (Fig. 5a).

304 Thicker ice in September tends thus to delay sea ice retreat, as expected. However, the conditions
305 in September (which integrate the effect of the perturbation in model physics since March in the
306 simulations started at that time) are not the only reason for the difference between the experiments
307 during the retreat season. The experiments starting in September from identical initial conditions tend
308 to diverge nearly immediately, indicating a larger control of sea ice physics on the evolution of the ice
309 extent at this time of the year compared to the advance season (Fig. 2cd).

310 This large role for sea ice physics in the melt season is illustrated by the larger differences between
311 the experiments for the timing of maximum of the ice melting than for the timing of maximum ice
312 growth rate (Fig. 4). The maximum ice melting rate spans a range of up to 50 days between the
313 experiments that have the earliest melting (AlbOce) and the latest one (ThickIce and No_Ice_Dyn). The
314 faster and earlier melting occurs in experiments AlbOce, as the low albedo in those experiments allows
315 a stronger absorption of incoming solar radiation and thus a larger amount of melt as soon as the Sun
316 is high enough above the horizon. In AlbOce experiments, a large part of the retreat is already achieved
317 by the end of November. This leads to a difference in ice extent that can reach more than 10 million
318 km² compared to the reference experiments at this time and thus a sea ice extent corresponding to
319 the one simulated only in early January in these reference experiments (Fig. 2). The ThinIce
320 experiments also display an earlier melting than ThickIce ones, reinforcing the direct effect of the
321 initially thinner ice in winter. This is due to a more efficient ice-albedo feedback: it is easier to melt
322 thin sea ice, leading to a higher amount of open water and thus a larger absorption of incoming solar
323 radiation and an intensified melting.

324 *Minimum extent, subsequent advance season and amplitude of the seasonal cycle*

325 Experiments with earlier melt onset and larger melt rates show faster retreat and lower minimum
326 extent, leading to a larger difference between the experiments in the first summer than in the first
327 winter. In the experiments starting in March, the range of ice extent across all experiments at the first
328 maximum reaches 1.2 million km² for NEMO and 1.9 million km² for PARASO. For the following
329 minimum in the same experiments, it reaches 3.6 million km² and 3.8 million km², respectively. The
330 numbers for the summer minimum are relatively similar for the experiments starting in September
331 compared to those starting in March, which suggests that processes in the summer season are more
332 important than the state of the sea ice-ocean-atmosphere system in September (Tables 2 and 3).

333 By contrast, the state of the sea ice-ocean-atmosphere system in March (i.e. the second year for
334 the experiments starting in March but already the first year for the experiments starting in September)
335 has a dominant influence during the whole sea ice advance season (Marchi et al., 2020). Despite the
336 strong control from the insolation and the limited direct impact of sea ice physics and feedbacks with
337 the ocean and the atmosphere during the first advance season (see above), the model physics
338 influences thus the evolution of the sea ice extent for several months during the second advance
339 season through their effect on the state of the system in March. This is illustrated in Fig. 5b by the
340 association between positive minimum sea ice extent anomaly and the subsequent positive maximum



341 extent anomalies present in most experiments, with the notable exception of NolceDyn experiments
342 as discussed below. In this figure, the minimum sea ice extent is chosen as a proxy for the state of the
343 sea ice and ocean system in summer but a similar link can be found for other variables, such as the
344 mean summer sea surface temperature southward of 60°S (Fig. S2).

345 The role of the state of the system in March can be illustrated for example using the Mix100
346 experiments. Increasing the vertical oceanic mixing in the sensitivity experiments redistributes the
347 available energy over the top 100 meters without modifying the vertically integrated heat content.
348 This does not have a large influence initially in the experiments starting in March (Fig. 2a). However,
349 the second year in the experiments starting in March is different from the first year as a deeper mixed
350 layer allows a larger heat uptake in summer. Consequently, the Mix100 experiments tend to have a
351 smaller ice extent than the reference experiments during the second sea ice advance season (Fig. 2a).

352 More generally, for both the coupled and uncoupled experiments, the summer extent influences
353 the whole advance season and the maximum extent. However, the difference in sea ice extent
354 between the experiments with NEMO tends to decrease with time because of the restoring imposed
355 by a fixed atmospheric state. For instance, the range in the maximum extent for the second year of the
356 experiments beginning in March reaches 2.1 million km² while it was 3.6 million km² the previous
357 summer (Fig. 2a). By contrast, the range between experiments increases during the sea ice advance
358 season in the PARASO experiments, reaching 4.8 million km² for the maximum extent in winter (25%
359 more than for the summer minimum).

360 While the majority of the experiments displaying a large winter ice extent also have a larger
361 summer ice extent, inducing relatively modest changes in the amplitude of the seasonal cycle, this is
362 not the case in the NolceDyn experiments. Those experiments are characterized by a reduced
363 amplitude of the seasonal cycle of the sea ice extent, with a smaller extent in winter and a larger one
364 in summer compared to the reference experiments. At the end of the advance season, the ice edge
365 position is set by the advection of sea ice from the south. Sea ice then melts in regions which are too
366 warm to sustain local production (e.g., Holland and Kimura, 2016; Nie et al., 2022). Neglecting ice
367 transport thus leads to an earlier maximum extent and onset of the retreat (Fig. 2). Later during the
368 retreat season, ice is transported northward where it melts and this transport also enhances the
369 formation of leads within the ice pack that increases solar absorption. Therefore, ice dynamics plays
370 an important role in accelerating the ice retreat, as shown in earlier studies (Fichefet and Morales
371 Maqueda, 1997; Holland and Kimura, 2016, Kusahara et al., 2019; Eayrs et al., 2020), and neglecting
372 this effect in NolceDyn induces an increase in the minimum ice extent of several million km² (Tables 2
373 and 3).

374 *Sensitivity to the starting date in NoMassFlux*

375 Neglecting brine release during ice formation (experiments NoMassFlux) reduces the heat input
376 from the deeper oceanic layer to the surface and results in a clear increase in ice production and
377 volume in the experiments started in March, in particular in coupled mode. It only has a limited
378 influence on the sea ice extent during the first winter as, by definition, it can only act after sea ice is
379 already present (Martinson, 1990). The effect can only be seen indirectly during the sea ice retreat
380 season (when entrainment no longer plays a clear direct role) and the second year, through the
381 influence of the perturbation on the sea ice volume. In particular, this leads to an increase in sea ice
382 extent in NoMassFlux_PARA_Mar of nearly 2.0 million km² compared with the corresponding
383 reference experiment in summer.

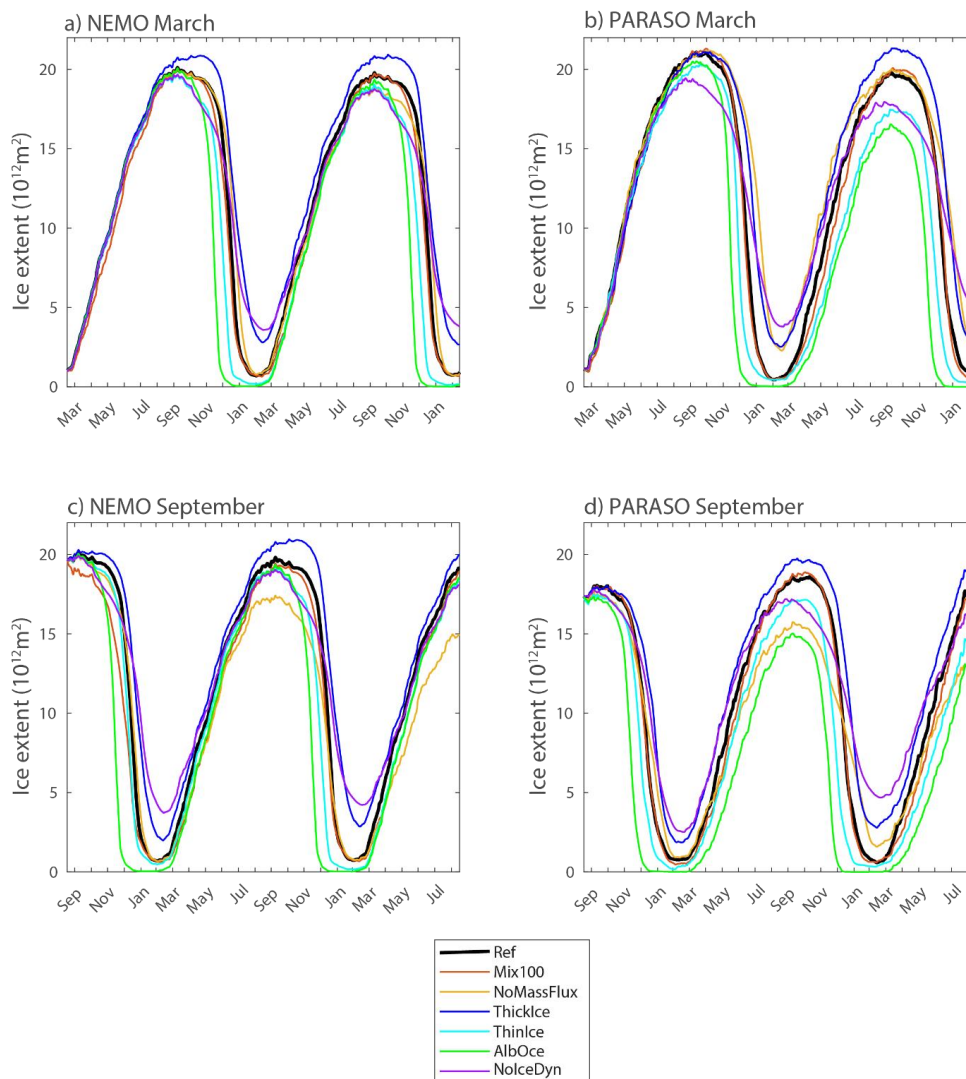
384 The NoMassFlux experiments starting in September have a different behavior than the
385 experiments beginning in March. As the model has a very low sea ice volume in March, assuming that



386 sea ice has the same salinity as the ocean does not substantially impact the salt and freshwater balance
387 of the model. In contrast, for the experiments starting in September, because of the much larger initial
388 sea ice volume, the NoMassFlux experiments imply a large artificial salt input in the system. The salt
389 input weakens the upper ocean stratification, enhances mixing and triggers open ocean convection
390 and the formation of open ocean polynyas (Fig. 6). This brings a large amount of heat to the ocean
391 surface, reducing both the sea ice volume and winter sea ice extent in NoMassFlux_NEMO_Sep and
392 NoMassFlux_Par_Sep compared with the corresponding reference experiments.

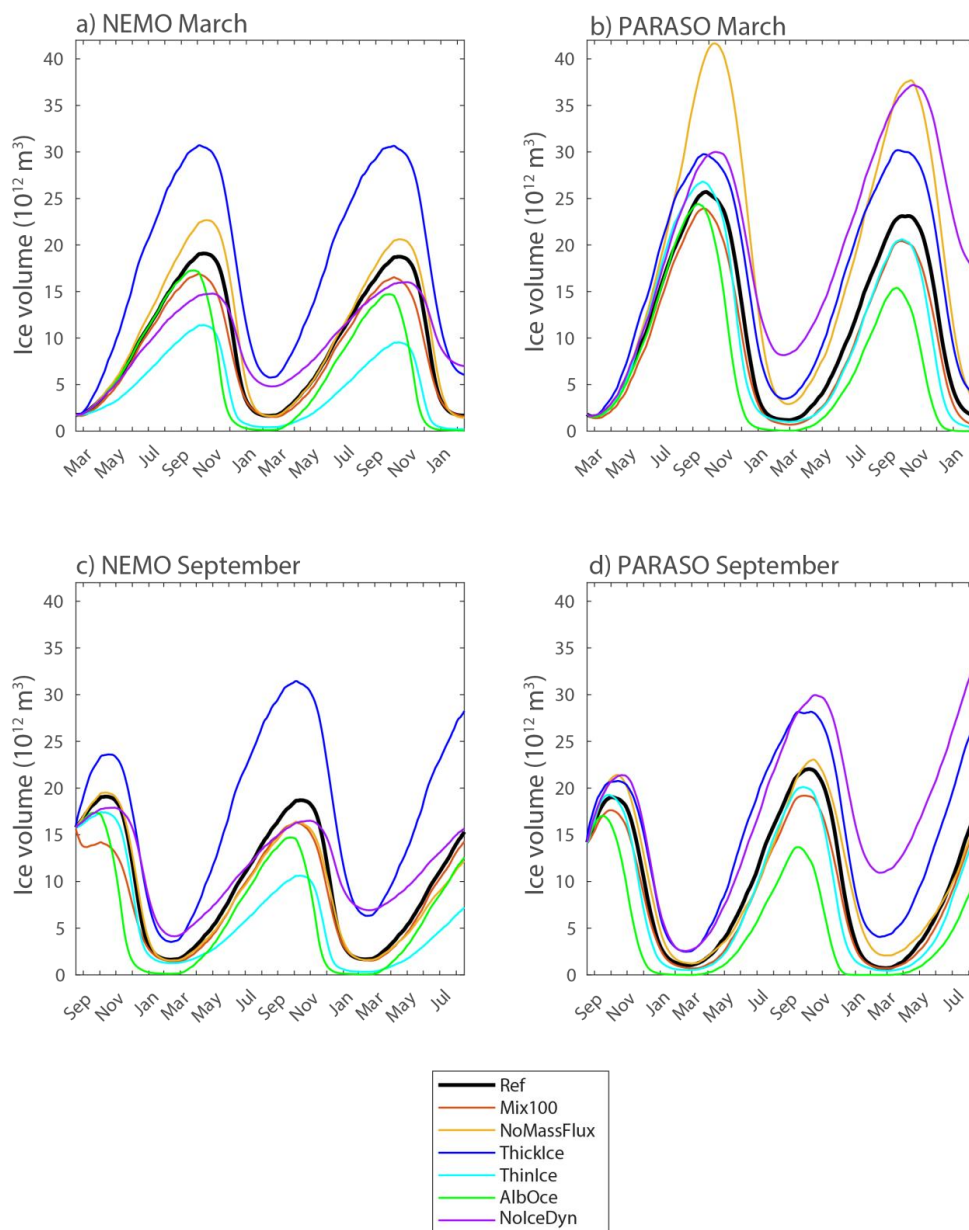
393 *Timing of the maximum and minimum extents*

394 Overall, as expected based on previous studies, the effect of the perturbations prescribed in our
395 sensitivity experiments is relatively modest on the timing of the minimum and maximum ice extents.
396 The largest signal arises in the sea ice dynamics perturbation, which tends to advance the date of
397 maximum in the coupled experiments (14 days and 12 days for the second maximum in
398 NolceDyn_PAR_Mar and NolceDyn_PAR_Sep, respectively), and in the experiment with perturbed
399 heat conduction, as the thicker pack can delay the maximum by up to 25 days (in ThickIce_NEMO_Sep).
400 Open ocean convection can also bring forward the date of the maximum with a third maximum already
401 achieved in day 230 and day 239 the second year in NoMassFlux_NEMO_Sep and
402 NoMassFlux_PAR_Sep (36 and 28 days earlier compared to the previous year of the same experiment,
403 respectively). The summer minimum can be advanced by up to 43 days in AlbOce_PAR_Sep through
404 the albedo decrease, and delayed by up to 18 days in the sea-ice dynamics deprived experiment
405 NolceDyn_NEMO_Sep. Note that some values in Tables 2 and 3 should be taken with caution as the
406 evolution of sea ice extent is relatively flat close to the maximum and small differences can produce
407 large shifts in the specific day of the maximum (e.g. in Mix100_PAR_Sep and ThinIce_PAR_Sep).



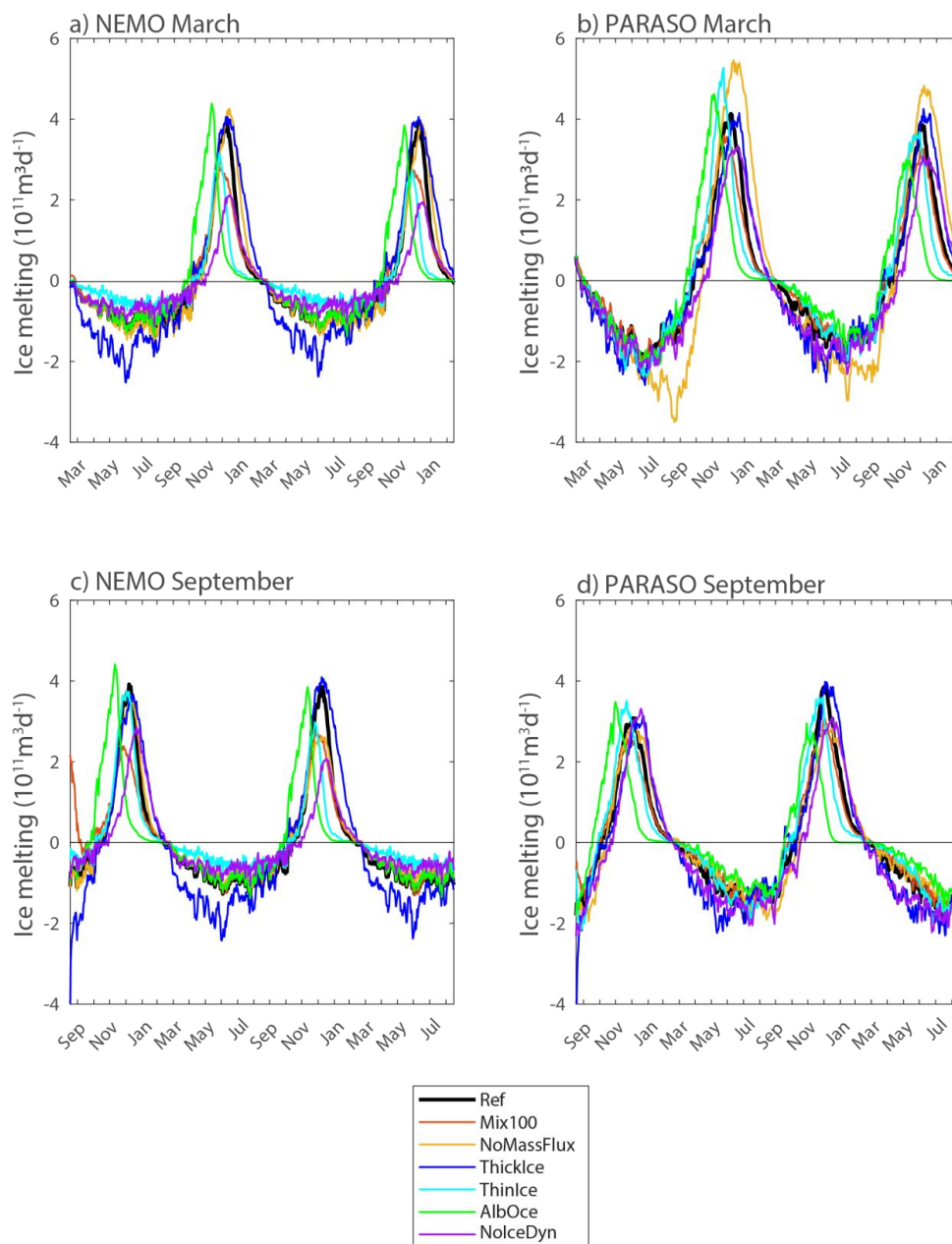
408
409
410
411
412

Figure 2. Antarctic sea ice extent (in 10^{12}m^2) in the group of experiments starting in March (top row) and September (bottom row) for the NEMO (left column) and PARASO configurations (right column).



413
414
415
416

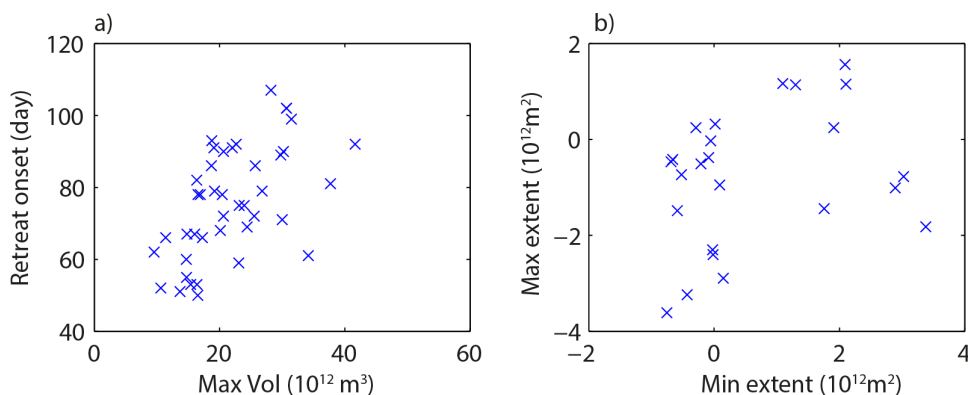
Figure 3. Antarctic sea ice volume (in 10^{12} m^3) in the group of experiments starting in March (top row) and September (bottom) for the NEMO (left column) and PARASO configurations (right column).



417

418 Figure 4. Mass flux due to sea ice growth and melt (counted positive for melting) integrated over
419 the Southern Ocean (in $10^{11} \text{m}^3 \text{d}^{-1}$) in the group of experiments starting in March (top row) and
420 September (bottom) for the NEMO (left column) and PARASO configurations (right column). This
421 diagnostic is evaluated online in NEMO from the different contributions to ice formation and melting
422 but is equivalent to the time derivative of the ice volume.

423



424

425 Figure 5. a) Onset of significant seasonal sea ice retreat (in day), defined as the number of days
 426 after the maximum at which the Antarctic sea ice extent has decreased to 95% of its maximum value
 427 as a function of the maximum ice volume (in 10^{12} m^3). b) Maximum sea ice extent anomaly (in 10^{12} m^2)
 428 compared to the reference experiment as a function of the anomaly in the previous minimum (in
 429 10^{12} m^2) for the second year of the experiments starting in March and for the first minimum and second
 430 maximum of the experiments starting in September.

431

432 Table 2. Values and timings of the maximum and minimum sea ice extents for the two years of the
 433 sensitivity experiments starting in March. Extents are given in 10^{12} m^2 and timings in Julian days.

	Year 1				Year 2			
	Max	Min	Day Max	Day Min	Max	Min	Day Max	Day Min
Ref_NEMO_Mar	20.1	0.70	265	46	19.8	0.73	266	47
Mix100_NEMO_Mar	20.0	0.64	265	57	19.8	0.66	266	57
NoMassFlux_NEMO_Mar	20.0	0.79	265	46	18.8	0.70	266	49
ThickIce_NEMO_Mar	20.9	2.80	265	58	20.9	2.66	291	58
ThinIce_NEMO_Mar	19.7	0.17	265	48	19.0	0.12	266	47
NoIceDyn_NEMO_Mar	19.7	3.59	265	59	18.8	3.58	266	60
AlbOce_NEMO_Mar	20.1	0.03	265	43	19.4	0.01	266	43
Ref_PAR_Mar	21.1	0.45	269	48	19.8	0.59	267	60
Mix100_PARA_Mar	21.3	0.46	286	48	20.1	0.37	269	57
NoMassFlux_PARA_Mar	21.2	2.36	294	59	20.0	2.29	267	63
ThickIce_PARA_Mar	21.1	2.54	294	59	21.3	2.45	267	59
ThinIce_PARA_Mar	20.3	0.42	276	48	17.5	0.23	264	50
NoIceDyn_PARA_Mar	19.4	3.82	249	59	17.9	3.79	253	65
AlbOce_PARA_Mar	20.5	0.02	269	57	16.5	0.00	265	30

434

435

436

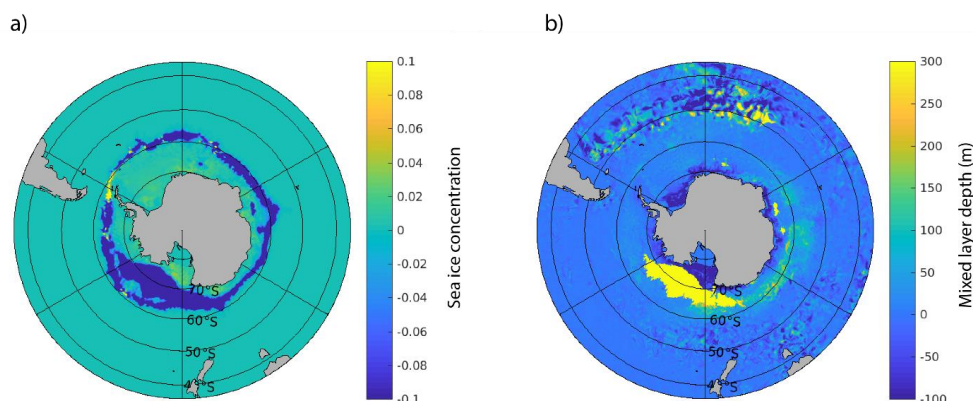
437



438 Table 3. Values and timings of the maximum and minimum sea ice extents for the two years of the
 439 sensitivity experiments starting in September. Extents are given in 10^{12} m² and timings in Julian days.

	Year 1				Year 2			
	Max	Min	Day Max	Day Min	Max	Min	Day Max	Day Min
Ref_NEMO_Sep	20.1	0.69	265	44	19.8	0.73	266	45
Mix100_NEMO_Sep	19.6	0.60	244	57	19.4	0.66	266	55
NoMassFlux_NEMO_Sep	19.9	0.67	265	49	17.4	0.69	266	47
ThickIce_NEMO_Sep	20.3	1.99	265	57	20.9	2.66	286	56
ThinIce_NEMO_Sep	20.0	0.48	265	44	19.3	0.12	266	44
NoIceDyn_NEMO_Sep	20.0	3.71	265	59	19.0	3.58	266	63
AlbOce_NEMO_Sep	20.0	0.03	265	44	19.3	0.01	266	41
Ref_PARA_Sep	18.0	0.76	268	56	18.6	0.58	267	58
Mix100_PARA_Sep	18.0	0.46	269	50	18.9	0.61	290	56
NoMassFlux_PARA_Sep	17.7	0.90	262	57	15.7	1.58	267	58
ThickIce_PARA_Sep	18.0	1.85	287	61	19.8	2.78	275	58
ThinIce_PARA_Sep	17.5	0.16	269	47	17.2	0.32	289	54
NoIceDyn_PARA_Sep	17.8	2.52	262	63	17.2	4.68	255	65
AlbOce_PARA_Sep	17.4	0.00	244	64	15.0	0.00	267	15

440



441

442 Figure 6. Differences in a) ice concentration and b) mixed layer depth (in m) in August of the second
 443 year of simulation between NoMassFlux_NEMO_Sep and the corresponding reference experiment.

444

445 4 Atmospheric feedbacks

446 The results discussed in Section 3 have highlighted differences between the NEMO and PARASO
 447 experiments and the role of the coupling with the atmosphere is further quantified here. In NEMO, the
 448 surface energy budget has only one degree of freedom (the surface temperature). Therefore, the
 449 surface readily adjusts to the forcing, so that the surface temperature closely follows the air
 450 temperature, which can be seen as a form of restoring. In PARASO, the surface energy budget responds
 451 to both sea ice and atmospheric processes. Another degree of freedom is now that the atmosphere



452 warms or cools in response to changes in sea ice, which in turn affects non-solar (downward longwave
453 and turbulent) fluxes.

454 This effect of the changes in the atmosphere is evaluated by computing atmospheric feedback
455 factors in response to the perturbation for each pair of coupled and uncoupled model experiments.
456 Feedbacks can be evaluated in different ways. A methodology that is consistent for a wide range of
457 feedbacks, including the standard radiative ones involved in computation of the so-called climate
458 sensitivity as well as non-radiative feedbacks, is to define the feedback factor γ as (Goosse et al., 2018):

$$459 \quad \gamma = \frac{\textit{Total Response} - \textit{Reference Response}}{\textit{Total Response}} \quad (1)$$

460 where the *Total Response* corresponds to the response of the model to some perturbation imposed in
461 the system when all the feedbacks are active, while the *Reference Response* is the response of the
462 model to the same imposed perturbation when one feedback or process to be studied (for instance
463 sea ice dynamics) has been left out. As our specific goal is to study the impact of atmospheric coupling,
464 this leads to:

$$465 \quad \gamma = \frac{\textit{Coupled Response} - \textit{Uncoupled Response}}{\textit{Coupled Response}} \quad (2)$$

466 and for sea ice extent specifically:

$$467 \quad \gamma_{SIE} = \frac{\Delta SIE_{PARA} - \Delta SIE_{NEMO}}{\Delta SIE_{PARA}} \quad (3)$$

468 where ΔSIE_{PARA} and ΔSIE_{NEMO} are the changes between the sensitivity experiments and the reference
469 experiments in the PARASO and NEMO configurations, respectively.

470 The feedback factor can be related to the feedback gain G (e.g., Goosse et al. 2018) defined here
471 as the ratio between the response in coupled mode and the one in uncoupled mode:

$$472 \quad G = \frac{\Delta SIE_{PARA}}{\Delta SIE_{NEMO}} = \frac{1}{1 - \gamma_{SIE}} \quad (4)$$

473 A negative value of γ thus corresponds to a negative feedback (changes in PARASO smaller than in
474 NEMO, feedback gain smaller than 1, and the feedback dampens the response to a perturbation); a
475 value between 0 and 1 corresponds to a positive feedback (changes in PARASO larger than in NEMO,
476 feedback gain larger than 1, the feedback amplifies the perturbation); a value of 1 implies an infinite
477 gain and values of γ larger than 1 imply a change in the sign of the response between coupled and
478 uncoupled model experiments (negative feedback gain). In the following, we start by discussing the
479 feedback factors lower than 1 (positive and negative feedbacks and positive feedback gains) that are
480 the easiest to interpret in a linear framework, while non-linearities and values of γ larger than one
481 (negative feedback gain) will be discussed in the last paragraphs of the section. We have not analyzed
482 the feedback factors when the coupled response is smaller than 0.2 million km² for sea ice extent or
483 0.2 thousand km³ for sea ice volume, corresponding to very small changes in the system and large
484 feedback factors (the coupled response appears in the denominator of γ). Consistently, we have
485 focused the analyses on the second year of the experiments, as for the first year the changes in several
486 experiments are too small.

487



488 *Atmospheric feedbacks on the maximum ice extent.*

489 The feedback factors are always positive for the maximum sea ice extent (Fig. 7a), indicating that
490 the coupling with the atmosphere amplifies the wintertime response to perturbations (for the
491 feedback factors smaller than 1, for the ones larger than 1 see below). This matches well our
492 understanding of the system, where sea ice acts as an insulator between the atmosphere and the
493 ocean. An increase in sea ice extent resulting from a perturbation thus cools the atmosphere, which
494 amplifies the initial change, giving a positive feedback. The same positive feedback mechanism applies
495 in the context of an initial decrease in ice extent, leading to atmospheric warming and additional
496 decrease in extent. For example, in AlbOce_PARA_Mar, the surface air temperature is higher than in
497 the reference experiment all year long. The difference reaches 1.5K on average over the two years of
498 the simulations for the oceanic region south of 60°S, and more than 2.5K in the second winter (Fig. 8,
499 Fig. S3).

500 Among all the experiments, AlbOce displays the largest feedback gain for the winter ice extent
501 (i.e. $\gamma < 1$ and closest to 1), with values of $\gamma = 0.87$ (Fig. 7a) in both experiments started in March and
502 September and hence a feedback gain of 7.7 (Fig. S4a). This is not surprising as the albedo changes
503 associated to sea ice variations are usually considered as a key characteristic of polar marine climates.
504 The sea-ice albedo feedback is already active in the NEMO configuration as a change in sea-ice
505 concentration affects the surface albedo and thus the net solar radiation absorbed at surface: in
506 AlbOce_NEMO_Mar and AlbOce_NEMO_Sep, the ocean-sea ice surface south of 60 S have a net solar
507 absorption higher than in their reference counterparts of 13 W m^{-2} in annual mean (Fig. S5). This is
508 even higher than in AlbOce_PARA_Mar and AlbOce_PARA_Sep, where the change reaches only
509 7 W m^{-2} . The higher values in the NEMO configuration might be due to differences in the mean state
510 between the coupled and uncoupled model configurations or to feedbacks related to clouds in
511 PARASO, but investigating those effects in more detail is out of the scope of the present study.
512 Nevertheless, the main difference between the coupled and uncoupled experiments comes from the
513 non-solar heat fluxes (Fig. S6), which is the net downward flux associated with incoming and outgoing
514 longwave radiation, and latent and sensible heat exchange with the atmosphere. In
515 AlbOce_NEMO_Mar and AlbOce_NEMO_Sep, as the atmospheric state is prescribed, the reduction in
516 sea ice extent and surface warming induce a large increase in non-solar heat losses that reaches 10
517 and 13 W m^{-2} averaged over the area south of 60°S, respectively. In other words, the artificial restoring
518 to the observed atmospheric state in uncoupled mode makes the non-solar heat loss at the surface
519 nearly compensate for the additional solar heat input. By contrast, the atmospheric warming in
520 AlbOce_PARA_Mar and AlbOce_PARA_Sep only leads to a moderate increase of the non-solar heat
521 losses, with annual mean values of 1 and 4 W m^{-2} , respectively. This explains the larger changes in ice
522 extent in coupled mode and the strong drift of the system to a warmer state (Fig. 8).

523 *Atmospheric feedbacks on maximum ice volume.*

524 The feedback factor for the winter volume is also positive in many experiments (Fig. 7b). In
525 particular, the value of γ in NoMassFlux_Mar equals 0.87, corresponding to a feedback gain G of 7.7.
526 In NoMassFlux experiments, the heat input from the ocean to the surface is reduced because of the
527 absence of the ice production–entrainment feedback. This increases ice production and thus ice
528 thickness. In the coupled model integration, the downward non-solar (net LW and turbulent) fluxes
529 can respond to thicker ice and colder surface, which further decreases the surface air temperature by
530 more than 3K in average over the oceanic region South of 60°S during the sea ice growth season. This
531 further enhances the ice production and leads then to a very strong positive atmospheric feedback.



532 By contrast, the atmosphere provides a negative feedback in the case of the ThinIce and ThickIce
533 experiments. Larger snow and ice thermal conductivities in ThickIce imply larger heat losses from the
534 ocean to the atmosphere in ice-covered regions and thus larger winter sea ice production in all the
535 ThickIce experiments (Fig. 4). In the PARASO configuration, the increased heat conduction from the
536 ice-ocean system warms the lower atmosphere in winter within the ice pack by more than 3K,
537 integrating over the region south of 60°S (Fig. 8). Consequently, the non-solar atmosphere-ice heat
538 fluxes can increase in coupled mode, moderating the increase in sea ice volume compared to the
539 NEMO experiments. In ThinIce, the smaller heat conduction fluxes induce an atmospheric cooling in
540 winter, located mainly close to the continent where the largest volume change occurs compared to
541 the reference experiment.

542 The experimental design in ThickIce and ThinIce may appear counterintuitive as our modifications
543 to the model physics warm the atmosphere when the ice is thicker. Such perturbations highlight a
544 coupling between heat conduction in the ice and non-solar downward atmospheric heat fluxes. When
545 the full system is considered in the real world, we rather experience the effects of the strong coupling
546 between thickness and heat conduction, often referred to as the ice growth-thickness feedback in
547 which an anomalously thin sea ice cover will lose more energy by conduction in winter, leading to a
548 thicker and colder ice, reducing the initial anomaly (Maykut, 1986; Bitz and Roe, 2004; Goosse et al.,
549 2018).

550 *Atmospheric feedbacks on minimum ice extent and volume.*

551 Positive feedback factors associated to the coupling with the atmosphere would also be expected
552 for the minimum ice extent (Fig 7c), in particular because of the amplifying role of the ice-albedo
553 feedback and its impact on air temperature. This is consistent with the highest summer air
554 temperature in the two experiments with the lowest summer ice extent (ThinIce and AlbOce, Fig. 8).
555 Accordingly, positive values are found in several experiments. However, negative values are also
556 obtained for others. This may be surprising in particular for AlbOce but this can be considered as an
557 artefact related to the methodology used to compute γ . All the sea ice melts in summer in the
558 experiments AlbOce (Figs. 2 and 3). The response is thus equal to the summer sea ice extent (or
559 volume) in the corresponding reference experiments. As this reference extent (and volume) is slightly
560 higher in NEMO configuration than in PARASO (Figs. 1 and 2), the response is larger in NEMO. This then
561 leads to a negative value of γ by definition (Eq. 3).

562 For ThinIce and ThickIce experiments, the negative atmospheric feedback factors obtained for the
563 summer ice volume (Fig 7d) are a direct consequence of the negative values discussed above for winter
564 ice volume in the same experiments, the winter sea ice thickness anomalies persisting until the
565 summer. As those anomalies are particularly large close to the coast, they affect the melting in those
566 regions and thus the feedback factor for the summer sea ice extent, leading to a negative value in
567 ThinIce and values very close to zero in the ThickIce experiments (Fig. 7c).

568 *Feedback factors larger than one: impact of the spatial distribution of the response.*

569 The analyses of the feedback factors illustrate the nonlinearity of the system, for example when
570 comparing the very different values of γ for an increase or a decrease in the conductivity in ThickIce
571 and ThinIce. Values of γ higher than one also suggest more complex dynamics than a simple
572 amplification or damping of the response by interactions with the atmosphere as even the sign of the
573 response is different between coupled and uncoupled model configurations. In many cases, this
574 different sign of the response integrated over the whole Southern Ocean, as measured on the anomaly
575 of total sea ice extent or ice volume, is due to a spatially heterogeneous response in uncoupled mode.

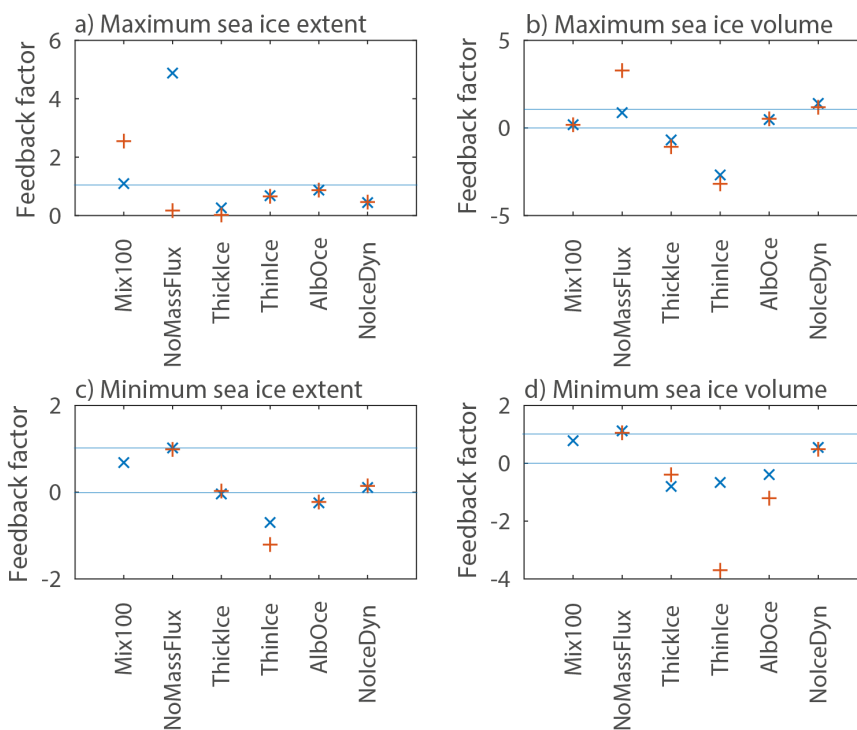


576 The coupling amplifies or damps the response locally as described by the feedback framework.
577 However, this may change the balance between positive and negative contributions and thus modify
578 the sign of the response integrated over the whole Southern Ocean compared to the uncoupled mode,
579 explaining the value of γ higher than 1.

580 We will not discuss here all the experiments displaying a value of γ higher than 1, especially
581 because in some cases the difference in the response to the coupling is small and thus probably not
582 very meaningful. Nevertheless, two examples seem illustrative and are detailed below. In NoIceDyn,
583 the sea ice thickness increases in winter close to the coast and decreases close to the ice edge
584 compared to the reference experiment, both in coupled and uncoupled mode (Fig. S7). The integrated
585 volume response is thus a balance between the changes in the two regions and, depending on their
586 relative strength, the sign of the change in ice volume can change. In coupled mode, the very large
587 increase in thickness close to the coast associated with strong local positive feedbacks with the
588 atmosphere dominates, while in the uncoupled mode, the offshore decrease dominates, then leading
589 to γ greater than 1 for winter ice volume.

590 At the time of the winter maximum in sea ice extent, sea ice is transported to the ice edge where
591 it tends to melt. The associated freshwater release increases the upper ocean stratification in the
592 reference experiment, reducing the oceanic heat input to the surface and thus favoring the advance
593 of the pack. (This positive feedback at the ice edge at the time of the maximum ice extent can be
594 contrasted with the negative ice production-entrainment feedback within the pack). In
595 NoMassFlux_NEMO_Mar, the absence of freshwater release during ice melt leads to a weaker upper
596 ocean stratification close to the ice edge, allowing deeper mixed layers, with a difference that can
597 reach more than 100m. As a consequence, the heat input from the ocean to the ice is higher. This is
598 sufficient to limit the seasonal sea ice advance and the maximum ice extent is lower in
599 NoMassFlux_NEMO_Mar than in the reference experiment by about 1 million km² in the second year
600 of the experiments (Fig. 2a). By contrast, the large increase in ice thickness and volume in
601 NoMassFlux_PARA_Mar discussed previously dominates the response even at the ice edge, leading to
602 a positive anomaly in the maximum ice extent. As a consequence, the atmospheric feedback factor is
603 greater than one. This effect is only seen in the experiments starting in March, as those starting in
604 September are dominated by the consequences of deep mixing and polynya formation within the pack.

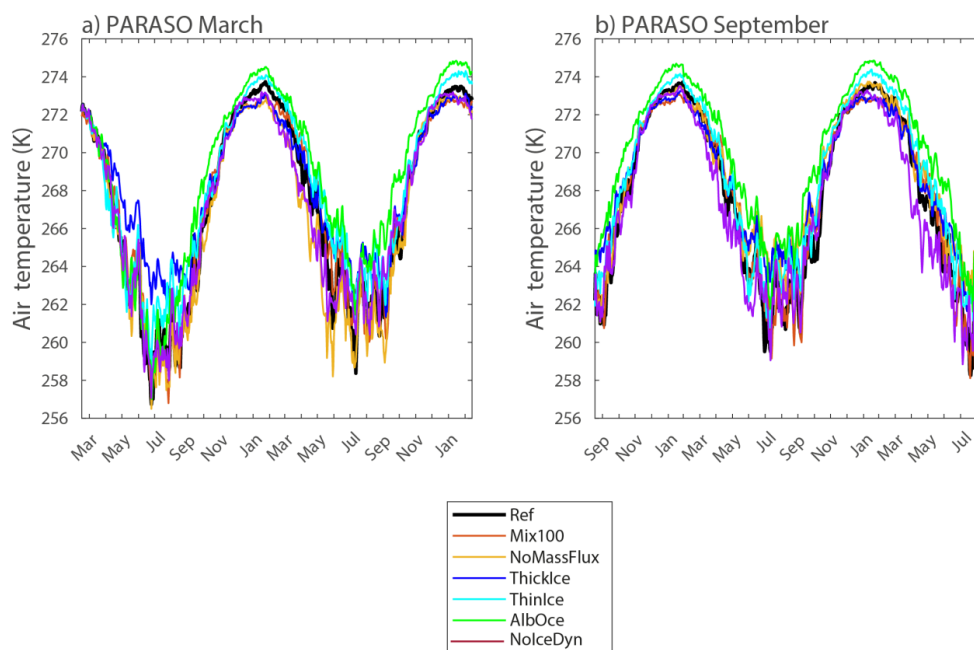
605



606

607 Figure 7. Atmospheric feedback factor for experiments starting in March (blue x) and September
 608 (red +) for a) the maximum sea ice extent, b) maximum sea ice volume, c) minimum sea ice extent and
 609 d) minimum sea ice volume. Light blue lines are drawn at values of 0 and 1 (with positive feedback
 610 between those two lines). The equivalent figure for the feedback gain G is given as Fig. S4.

611



612

613 Figure 8. Surface air temperature (in K) averaged over the oceanic region south of 60°S in the
614 group of experiments starting a) in March and b) in September for the PARASO configuration.

615

616 5 Discussion and conclusions

617 We have performed a series of 24 sensitivity experiments to analyze the role of key sea ice
618 processes and coupling mechanisms between sea ice, ocean and atmosphere in driving the seasonal
619 cycle of the Antarctic sea ice extent. In order to obtain clear signals and identify the mechanisms at
620 play, deliberately strong and idealized perturbations have been used in our simulations. One limiting
621 aspect arising from making such a design choice is the resulting lack of ability to directly compare the
622 experiments with observational datasets. Furthermore, our quantitative results may be model-
623 dependent, as they can be influenced by the way physical processes are represented in the models
624 and by the biases in the model mean state, which can have a strong influence on the response of
625 models to perturbations (e.g. Goosse et al., 2018; Massonnet et al., 2018). Additionally, the
626 experimental design itself may have an impact on the way some of the processes are evaluated.
627 However, we consider that the relative importance of the different processes and their description are
628 robust and we will thus focus on those aspects here.

629 Recall that all the simulations used the same atmospheric forcing (for NEMO simulations) or the
630 same conditions at the boundaries of the domain of the regional atmospheric model that significantly
631 constrain the seasonal evolution of the sea ice (PARASO simulations). Changes in the large-scale
632 atmospheric conditions or in the passage of synoptic storms close to the ice edge, for instance, are
633 known to have a strong impact on the evolution of the ice extent (e.g., Handcock and Raphael, 2020).
634 While this role of the atmospheric variability is not addressed here, the analyses of the processes at
635 play could provide insight for understanding how the ice-ocean system responds to interannual
636 variations of the atmospheric conditions. For instance, our results are consistent with the large role



637 attributed to the sea ice dynamics and thus to the interannual variability in winds in driving changes in
638 sea ice extent anomalies during the retreat season (e.g., Kushara et al., 2019; Eayrs et al., 2020)

639 Our experiments are too idealized to provide explicit recommendations for model improvements
640 but the identification of the key processes can help to target the changes that might have the largest
641 impact. In particular, the delayed onset of the seasonal sea ice retreat after the maximum present in
642 our simulations can possibly be related to a too thick ice cover, which may be associated with a
643 misrepresentation of processes in the marginal ice zone (Roach et al., 2018, 2019; Alberello et al., 2020;
644 Horvat, 2021).

645 We have focused on the sea ice extent integrated over the whole Southern Ocean, although the
646 net influence of a process may be the result of opposite effects between sectors of the Southern Ocean
647 or between coastal regions and the open ocean. For instance, removing ice dynamics tends to increase
648 the ice thickness close to the coast and decrease it at the sea ice edge because of a reduced ice
649 transport, with a clear impact on the temperature changes. This is an illustration that our conclusions
650 derived for the whole ice pack are not necessarily valid for a specific region.

651 Overall, our results confirm the earlier finding that the model physics have only a moderate effect
652 on the timings of the maximum and minimum Antarctic sea ice extents, which are rather controlled by
653 the insolation cycle (Roach et al., 2022). Deactivating the sea ice dynamics in our models induces an
654 earlier maximum and a tendency towards a later minimum, but the shift is at maximum of the order
655 of one week or two, which is within the range of year-to-year fluctuations in the observed record.
656 Thicker ice can delay the maximum and a lower albedo lead to an earlier minimum, but similarly this
657 does not strongly modify the shape of the seasonal cycle, in particular its asymmetry. Our experiments
658 are only 2 years in length and there is a possibility that the shifts would become larger at equilibrium,
659 but in the experiments featuring a clear drift (such as NolceDyn_PAR and AlbOce_PAR), we observe a
660 change in the values of the maximum and minimum ice extents from the first to the second year rather
661 than on their timing. The only exception is related to strong open ocean convection that can stop the
662 ice advance season efficiently when it is triggered in the model.

663 Nevertheless, our results demonstrate that sea ice physics and interactions with the atmosphere
664 and ocean control many other aspects of the seasonal cycle of the ice extent, such as the values of the
665 maximum and minimum and the speed of the retreat. They thus strongly modulate the overall impact
666 of the sea ice in the climate system, in particular on the radiative balance through the modification of
667 the surface albedo and on the exchanges of heat and carbon between the ocean and atmosphere.

668 Our sensitivity experiments have also illustrated clear distinctions between the dynamics of the
669 sea ice advance and retreat seasons. The sea ice extent advance from March to August is nearly
670 insensitive to the perturbations applied, with nearly identical evolution of the sea ice extent in our
671 experiment over this period if they start from the same initial conditions in March. If the conditions
672 are different in March (e.g., inherited from differences during the previous melting season), this has
673 an effect during the whole advance season. We can interpret those results in the following way. The
674 very weak incoming solar radiation between March and August imposes a large heat loss over the
675 Southern Ocean and the response of the system depends more on the heat available in March (and
676 thus of conditions at that time) than on any other element in the system. However, the sea ice
677 processes during the ice advance season can have an indirect effect by changing the sea ice thickness
678 and modifying the sea ice extent later in the year. This is the case for the ice production-entrainment
679 feedback that limits the ice growth in winter. During the ice advance season, this has no major impact
680 on the ice extent itself as it modulates the characteristics of sea ice that is already present, but the
681 modification of the thickness has an influence later during the retreat.



682 The timing of the beginning of the seasonal sea ice retreat and its rate also depend on the late
683 winter conditions, with thicker ice melting later. However, the retreat rate differs strongly between
684 the experiments, and this may have a larger impact on the spring and summer ice extents than the
685 conditions in September. Among all the processes influencing the retreat rate, the ice albedo feedback
686 is the dominant one, with a lower albedo, whether it is induced directly by a change in albedo (AlbOce)
687 or indirectly by a thinner ice (ThinIce) that melts faster, strongly accelerating the ice retreat. The ice
688 transport also plays a clear role by transporting sea ice northward where it melts. Neglecting this
689 process therefore leads to a large increase in summer ice extent. This larger dependence on several
690 key physical processes during the seasonal ice retreat is consistent with the larger climate model
691 sensitivity to changes in parameters in spring and early summer than during the ice advance season
692 (e.g., Urrego-Blanco et al., 2016; Schroeter and Sandery, 2022) and with the larger interannual
693 variability in the melt rates observed over the satellite period than in the growth rates (e.g., Eayrs et
694 al., 2020).

695 From a prediction point of view, the findings of this paper are also consistent with the idea that
696 the seasonal predictability of Antarctic sea ice extent depends on the season itself (Chevallier et al.,
697 2019; Marchi et al., 2020). A diagnostic predictability study using satellite data has revealed that
698 February is the month for which the sea ice extent anomalies exhibit the largest autocorrelations for
699 all lead times up to 55 days (Chevallier et al., 2019). This is in line with our findings showing that the
700 seasonal development of sea ice extent during the growing season is minimally controlled by physics
701 but rather by insolation and initial conditions. By contrast, the lowest autocorrelations of sea ice extent
702 anomalies are reached in the melting season, with complete loss of predictability in mid-November.
703 This is again in line with our results that multiple physical factors control the dynamics of sea ice melt.

704 The impact of all the sea ice and oceanic processes investigated here on the ice extent in winter
705 are amplified by the coupling with the atmosphere and our experimental design allow us to quantify
706 this amplification. The largest winter atmospheric feedback occurs for perturbations in albedo, as this
707 strongly modifies atmospheric temperature and humidity, amplifying the response of the ice. The
708 effect of the ice production-entrainment feedback is also strongly amplified by the atmospheric
709 coupling, as it brings thermal energy to the surface that melts ice but also warm up the atmosphere,
710 increasing the response of sea ice. By contrast, negative atmospheric feedbacks can develop for the
711 ice thickness and volume. In particular, larger heat losses due to higher conductive heat fluxes through
712 the sea ice can lead to greater sea ice formation. This induces a larger thermal energy transfer from
713 the ice-ocean system to the atmosphere that reduces the initial heat loss, resulting in a negative
714 atmospheric feedback on the thickness and potentially on the summer extent.

715 Roach et al. (2022) identified the role of insolation in controlling the observed asymmetry in the
716 growing and melting of Antarctic sea ice. Our idealized sensitivity experiments show that within this
717 robust cycle, the melt rate and maximum and minimum sea ice extents can be affected by sea ice-
718 ocean exchanges, sea ice processes, and ice dynamics. We also demonstrated quantitatively how
719 atmospheric feedback can enhance the effect of perturbations, but also in some cases damp it.
720 Although it is an idealized study, it highlights the major role of albedo and sea ice transport in the sea
721 ice extent seasonal cycle and as key processes to target in model development and process
722 understanding.

723 **Code and data availability**

724 As described in detail in Pelletier et al. (2022a), the PARASO sources can be obtained by CLM-
725 Community members on their RedC (<https://redc.clm-community.eu/> then “COSMO-CLM” then
726 “Downloads”). All PARASO sources, except the COSMO routines, are publicly available for didactic



727 purposes at <https://doi.org/10.5281/zenodo.5576201> (Pelletier et al., 2021) as well as the files to run
728 the model in the same configuration as here (Pelletier and Helsen, 2021). The NEMO3.6 version is
729 available from <https://forge.ipsl.jussieu.fr/nemo/browser/branches/UKMO> (Mathiot and Storkey,
730 2018).

731 **Supplement link:**

732 Supplementary information is available as a separate file.

733 **Author contributions.** HG initiated the study and designed the sensitivity experiments after
734 discussions with all the co-authors. FK performed the simulations. FK and PVH prepared the model
735 outputs for the analyses. HG made the analyses and the figures and all the co-authors contribute in
736 the interpretation of the results. HG wrote the manuscript, with inputs from all co-authors

737 **Competing interests:**

738 The authors declare that they have no conflict of interest.

739 **Acknowledgements.** This work was performed in the framework of the PARAMOUR project,
740 “Decadal predictability and variability of polar climate: the role of atmosphere-ocean-cryosphere
741 multiscale interactions”, supported by the Fonds de la Recherche Scientifique – FNRS and the FWO
742 under the Excellence of Science (EOS) program (grant no. 00100718F, EOS ID no. 30454083). The
743 computational resources were provided by the VSC (Flemish Supercomputer Center), funded by the
744 Research Foundation Flanders (FWO) and the Flemish Government, the Center for High Performance
745 Computing and Mass Storage (CISM) of the Université catholique de Louvain (CISM/UCL) and the
746 Consortium des Équipements de Calcul Intensif en Fédération Wallonie Bruxelles (CÉCI), funded by the
747 Fond de la Recherche Scientifique de Belgique (F.R.S.-FNRS) under convention 2.5020.11 and by the
748 Walloon region. HG is research director with the F.R.S.-FNRS. EBW was supported by the Office of
749 Naval Research-DRI grant N00014-18-1-2175. LR was supported by the National Oceanic and
750 Atmospheric Administration (NOAA) Climate and Global Change Postdoctoral Fellowship Program,
751 which is administered by UCAR’s Cooperative Programs for the Advancement of Earth System Science
752 (CPAESS) under award NA18NWS4620043B.

753



754 References

- 755 Alberello, A., Bennetts, L., Heil, P., Eayrs, C., Vichi, M., MacHutchon, K., Onorato, M., and Toffoli,
756 A.: Drift of pancake ice floes in the winter antarctic marginal ice zone during polar cyclones, J.
757 Geophys. Res.—Oceans 125, e2019JC015418, 2020.
- 758 Barthélemy, A., Fichefet, T., Goosse, H., and Madec, G.: Modelling the interplay between sea ice
759 formation and the oceanic mixed layer: limitations of simple brine rejection parameterizations.
760 Ocean Modelling 86, 141-152, 2015.
- 761 Bitz, C. M. and Lipscomb, W. H.: An energy-conserving thermodynamic model of sea ice, J.
762 Geophys. Res.—Oceans, 104, 15669–15677, <https://doi.org/10.1029/1999JC900100>, 1999.
- 763 Bitz, C. M., Holland, M. M., Weaver, A. J., and Eby, M.: Simulating the ice-thickness distribution
764 in a coupled climate model, J. Geophys. Res.—Oceans, 106, 2441–2463,
765 <https://doi.org/10.1029/1999JC000113>, 2001.
- 766 Bitz, C. M. and Roe, G. H.: A mechanism for the high rate of sea ice thinning in the Arctic Ocean,
767 J. Clim. 17, 3623–3632, 2004.
- 768 Bouillon, S., Fichefet, T., Legat, V., and Madec, G.: The elastic–viscous–plastic method revisited,
769 Ocean Model., 71, 2–12, <https://doi.org/10.1016/j.ocemod.2013.05.013>, 2013.
- 770 Brandt, R. E., Warren, S. G., Worby, A. P., and Grenfell, T. C.: Surface Albedo of the Antarctic Sea
771 Ice Zone, J. Climate, 18, 3606–3622, <https://doi.org/10.1175/JCLI3489.1>, 2005.
- 772 Chevallier, M., Massonnet, F., Goessling, H., Guémas, V., and Jung, T.: The Role of Sea Ice in Sub-
773 seasonal Predictability, In Sub-Seasonal to Seasonal Prediction, 201–221, Elsevier.
774 <https://doi.org/10.1016/B978-0-12-811714-9.00010-3>, 2019.
- 775 Doms, G., Förstner, J., Heise, E., Herzog, H.-J., Mironov, D., Raschendorfer, M., Renhardt, T.,
776 Ritter, B., Schrodin, R., Schulz, J.-P., and Vogel, G.: COSMO-Model Version 5.05: A Description of the
777 Nonhydrostatic Regional COSMO-Model – Part I: Dynamics and Numerics, Tech. rep., Consortium for
778 Small-Scale Modelling, https://doi.org/10.5676/DWD_PUB/NWV/COSMODOC_5.05_II, 2018.
- 779 Downes, S.M., Farneti, R., Uotila, P., Griffies, S.M., Marsland, S.J., Bailey, D., Behrens, E.,
780 Bentsen, M., Bi, D., Biastoch, A., Böning, C., Bozec, A., Canuto, V.M., Chassignet, E., Danabasoglu, G.,
781 Danilov, S., Diansky, N., Drange, H., Fogli, P.G., Gusev, A., Howard, A., Ilicak, M., Jung, T., Kelley, M.,
782 Large, W.G., Leboissetier, A., Long, M., Jianhua, L., Masina, S., Mishra, A., Antonio Navarra, A.J.,
783 Nurser, G., Patara, L., Samuels, B.L., Sidorenko, D., Spence, P., Tsujino, H., Wang, Q., and Yeager, S.G.:
784 An assessment of southern ocean water masses and sea ice during 1988–2007 in a suite of
785 interannual core-ii simulations, Ocean. Modell. 94:67–94. <https://doi.org/10.1016/j.ocemod.2015.07.022>, 2015.
- 787 Eayrs, C., Holland, D. M., Francis, D., Wagner, T. J. W., Kumar, R., and Li, X.: Understanding the
788 seasonal cycle of Antarctic sea ice extent in the context of longer-term variability, Rev. Geophys., 57.
789 <https://doi.org/10.1029/2018RG000631>, 2019.
- 790 Eayrs, C., Faller D, and Holland D.M. Mechanisms driving the asymmetric seasonal cycle of
791 Antarctic Sea Ice in the CESM Large Ensemble, Ann. Glac. 1–10. <https://doi.org/10.1017/aog.2020.26>,
792 2020
- 793 Enomoto, H., and Ohmura, A.: The influences of atmospheric half-yearly cycle on the sea ice
794 extent in the Antarctic, J. Geophys. Res. 95, 9497, 1990.
- 795 Fetterer, F., Knowles, K., Meier, W. N., Savoie, M., and Windnagel, A. K.: Sea Ice Index, Version 3
796 [Data Set]. Boulder, Colorado USA. National Snow and Ice Data Center.
797 <https://nsidc.org/data/g02135/versions/3>, 2017.
- 798 Fichefet, T., and Morales Maqueda, M.A.: Sensitivity of a global sea ice model to the treatment
799 of ice thermodynamics and dynamics, J. Geophys. Res., 102(C6), 12,609–12,646, 1997.



- 800 Gaspar, P., Grégoris, Y., and Lefevre, J.-M.: A simple eddy kinetic energy model for simulations of
801 the oceanic vertical mixing: Tests at station Papa and long-term upper ocean study site, *J. Geophys.*
802 *Res.-Oceans*, 95, 16179–16193, <https://doi.org/10.1029/JC095iC09p16179>, 1990.
- 803 Gousse, H., Kay, J. E., Armour, K., Bodas-Salcedo, A., Chepfer, H., Docquier, D., Jonko, A.,
804 Kushner, P. J., Lecomte, O., Massonnet, F., Park, H.-S., Pithan, F., Svensson, G., Vancoppenolle, M.:
805 Quantifying climate feedbacks in polar regions, *Nat. Comm.* 9, 1919, DOI: 10.1038/s41467-018-
806 04173-0, 2018.
- 807 Gordon, A. L.: Seasonality of Southern Ocean sea ice, *J. Geophys. Res.* 86, 4193–4198, 1981.
- 808 Grenfell, T. C. and Perovich, D. K.: Seasonal and spatial evolution of albedo in a snow-ice-land-
809 ocean environment, *J. Geophys. Res.-Oceans*, 109, 8044, <https://doi.org/10.1029/2003JC001866>,
810 2004.
- 811 Handcock, M.S., and Raphael, M. N.: Modeling the annual cycle of daily Antarctic sea ice extent.
812 *The Cryosphere*, 14, 2159–2172, 2020, <https://doi.org/10.5194/tc-14-2159-2020>, 2020.
- 813 Hersbach, H., Bell, B., Berrisford, P., Hirahara, S., Horányi, A., Muñoz-Sabater, J., Nicolas, J.,
814 Peubey, C., Radu, R., Schepers, D., Simmons, A., Soci, C., Abdalla, S., Abellan, X., Balsamo, G.,
815 Bechtold, P., Biavati, G., Bidlot, J., Bonavita, M., De Chiara, G., Dahlgren, P., Dee, D., Diamantakis, M.,
816 Dragani, R., Flemming, J., Forbes, R., Fuentes, M., Geer, A., Haimberger, L., Healy, S., Hogan, R. J.,
817 Hólm, E., Janisková, M., Keeley, S., Laloyaux, P., Lopez, P., Lupu, C., Radnoti, G., de Rosnay, P., Rozum,
818 I., Vamborg, F., Villaume, S., and Thépaut, J.-N.: The ERA5 global reanalysis, *Q. J. Roy. Meteor. Soc.*,
819 146, 1999–2049, <https://doi.org/10.1002/qj.3803>, 2020.
- 820 Hobbs, W. R., Massom, R., Stammerjohn, S., Reid, P., Williams, G., and Meier, W.: A review of
821 recent changes in Southern Ocean sea ice, their drivers and forcings, *Global and Planetary Change*,
822 143, 228–250, 10.1016/j.gloplacha.2016.06.008, 2016.
- 823 Holland, P.R., and Kimura, N.: Observed Concentration Budgets of Arctic and Antarctic Sea Ice, *J.*
824 *Clim.*, 29 5241–6249, 2016.
- 825 Horvat, C: Marginal ice zone fraction benchmarks sea ice and climate model skill, *Nat. Commun.*
826 12, 2221, <https://doi.org/10.1038/s41467-021-22004-7>, 2021.
- 827 Kacimi, S., and Kwok, R.: The Antarctic sea ice cover from ICESat-2 and CryoSat-2: freeboard,
828 snow depth, and ice thickness. *The Cryosphere* 14, 4453–4474, 10.5194/tc-14-4453-2020, 2020.
- 829 Kusahara, K., Williams, G., Massom, R., Reid, P., and Hasumi, H.: Spatiotemporal dependence of
830 Antarctic sea ice variability to dynamic and thermodynamic forcing: A coupled ocean–sea ice model
831 study, *Clim. Dynam.*, 52, 3791–3807, <https://doi.org/10.1007/s00382-018-4348-3>, 2019.
- 832 Large, W. G., and Yeager, S. G: Diurnal to decadal global forcing for ocean and sea-ice models:
833 The data sets and flux climatologies, Tech. Rep., National Center for Atmospheric Research.,
834 <https://doi.org/10.5065/D6KK98Q6>, 2004.
- 835 Lazar, A., Madec, G., and Delecluse, P.: The deep interior downwelling, the Veronis effect, and
836 mesoscale tracer transport parameterizations in an OGCM, *J. Phys. Oceanogr.*, 29, 2945–2961.
837 [https://doi.org/10.1175/1520-0485\(1999\)029%3C2945:TDIDTV%3E2.0.CO;2](https://doi.org/10.1175/1520-0485(1999)029%3C2945:TDIDTV%3E2.0.CO;2), 1999.
- 838 Madec, G., Bourdallé-Badie, R., Bouttier, P.-A., Bricaud, C., Bruciaferri, D., Calvert, D., Chanut, J.,
839 Clementi, E., Coward, A., Delrosso, D., Ethé, C., Flavoni, S., Graham, T., Harle, J., Iovino, D., Lea, D.,
840 Lévy, C., Lovato, T., Martin, N., Masson, S., Mocavero, S., Paul, J., Rousset, C., Storkey, D., Storto, A.,
841 and Vancoppenolle, M.: NEMO ocean engine, Tech. rep., Insitut Pierre-Simon Laplace, Zenodo [code],
842 <https://doi.org/10.5281/zenodo.3248739>, 2017.
- 843 Marchi, S., Fichet, T., Gousse, H.: influence of the initial ocean state on the predictability of the
844 Antarctic sea ice at the seasonal timescale: a study with NEMO3.6-LIM3. *Ocean Modelling* 148,
845 101591, <https://doi.org/10.1016/j.ocemod.2020.101591>, 2020.
- 846 Martinson, D. G.: Evolution of the Southern Ocean winter mixed layer and sea ice-open ocean
847 deep-water formation and ventilation, *J. Geophys. Res. Oceans* 95, 11641–11654, 1990.



- 848 Massom, R., Reid, P., Stammerjohn, S., Raymond, B., Fraser, A., Ushio, S.: Change and variability
849 in East Antarctic sea ice seasonality, 1979/80–2009/10. *PLoS ONE*. [https](https://doi.org/10.1371/journal.pone.0064756)
850 [://doi.org/10.1371/journal.pone.0064756](https://doi.org/10.1371/journal.pone.0064756), 2013.
- 851 Massonnet, F., Vancoppenolle, M., Goosse, H., Docquier, D., Fichefet, T., Blanchard-
852 Wrigglesworth, E., and Bitz, C. M.: Arctic sea-ice variability tied to its mean state through
853 thermodynamic feedbacks. *Nature Climate Change*, 8, 599–603, [10.1038/s41558-018-0204-z](https://doi.org/10.1038/s41558-018-0204-z), 2018.
- 854 Massonnet, F., Barthélemy, A., Worou, K., Fichefet, T., Vancoppenolle, M., Rousset, C., and
855 Moreno-Chamarro, E.: On the discretization of the ice thickness distribution in the NEMO3.6-LIM3
856 global ocean–sea ice model, *Geosci. Model Dev.*, 12, 3745–3758, [https://doi.org/10.5194/gmd-12-](https://doi.org/10.5194/gmd-12-3745-2019)
857 [3745-2019](https://doi.org/10.5194/gmd-12-3745-2019), 2019.
- 858 Mathiot, P., Jenkins, A., Harris, C., and Madec, G.: Explicit representation and parametrised
859 impacts of under ice shelf seas in the z - coordinate ocean model NEMO 3.6, *Geosci. Model Dev.*, 10,
860 2849–2874, <https://doi.org/10.5194/gmd-10-2849-2017>, 2017.
- 861 Mathiot, P. and Storkey, D.: NEMO model code, MetOffice (UK) branch
862 `dev_isf_remapping_UKESM_GO6package_r9314`, revision 11248, MetOffice [code], available at:
863 [https://forge.ipsl.jussieu.fr/nemo/browser/branches/UKMO/dev_isf_remapping_UKESM_GO6packa](https://forge.ipsl.jussieu.fr/nemo/browser/branches/UKMO/dev_isf_remapping_UKESM_GO6package_r9314?rev=15667)
864 [ge_r9314?rev=15667](https://forge.ipsl.jussieu.fr/nemo/browser/branches/UKMO/dev_isf_remapping_UKESM_GO6package_r9314?rev=15667) (last access 21 January 2022), 2018.
- 865 Maykut, G. A. The surface heat and mass balance. *The Geophysics of Sea Ice* (ed. Untersteiner,
866 N.), Plenum Press, 395–464, 1986.
- 867 Nie, Y., Uotila, P., Cheng, B., Massonnet, F., Kimura, N., Cipollone, A., Lv, X. : Southern Ocean sea
868 ice concentration budgets of five ocean-sea ice reanalyses, *Clim. Dyn.* [https://doi.org/10.1007/s00382-](https://doi.org/10.1007/s00382-022-06260-x)
869 [022-06260-x](https://doi.org/10.1007/s00382-022-06260-x), 2022.
- 870 Nihashi, S., and Cavalieri, D. J.: Observational evidence of a hemispheric-wide ice–ocean albedo
871 feedback effect on Antarctic sea-ice decay. *Journal of Geophysical Research*, 111, C12001.
872 <https://doi.org/10.1029/2005JC003447>, 2006.
- 873 Oleson, K. W., Lawrence, D. M., Bonan, G. B., Drewniak, B., Huang, M., Koven, C. D., Levis, S., Li,
874 F., Riley, W. J., Subin, Z. M., Swenson, S. C., Thornton, P. E., Bozbiyik, A., Fisher, R., Heald, C. L.,
875 Kluzek, E., Lamarque, J.-F., Lawrence, P. J., Leung, L. R., Lipscomb, W., Muszala, S., Ricciuto, D. M.,
876 Sacks, W., Sun, Y., Tang, J., and Yang, Z.-L.: Technical Description of version 4.5 of the Community
877 Land Model (CLM), Tech. Rep. July, NCAR, available at:
878 http://www.cesm.ucar.edu/models/cesm1.2/clm/CLM45_Tech_Note.pdf (last access: 21 January
879 2022), 2013.
- 880 Parkinson, C.L.: Global Sea Ice Coverage from Satellite Data: Annual Cycle and 35-Yr Trends. *J.*
881 *Clim.* 27, 9377–9382, 2014.
- 882 Parkinson, C. L.: A 40-y record reveals gradual Antarctic sea ice increases followed by decreases
883 at rates far exceeding the rates seen in the Arctic, *Proc. Nat. Acad. Sciences* 116, 14414–14423,
884 [10.1073/pnas.1906556116](https://doi.org/10.1073/pnas.1906556116), 2019.
- 885 Pelletier, C. and Helsen, S.: PARASO ERA5 forcings, Zenodo [dataset],
886 <https://doi.org/10.5281/zenodo.5590053>, 2021.
- 887 Pelletier, C., Klein, F., Zipf, L., Haubner, K., Mathiot, P., Pattyn, F., Moravveji, E., and Vanden
888 Broucke, S.: PARASO source code (no COSMO), Zenodo [code],
889 <https://doi.org/10.5281/zenodo.5576201>, 2021.
- 890 Pelletier C., Fichefet, T., Goosse, H., Haubner, K., Helsen, S., Huot, P.-V., Kittel, C., Klein, F., Le
891 clec'h, S., van Lipzig, N. P. M., Marchi, S., Massonnet, F., Mathiot, P., Moravveji, E., Moreno, E.,
892 Ortega, P., Pattyn, F., Souverijns, N., Van Achter, G., Vanden Broucke, S., Vanhulle, A., Verfaillie, D.,
893 and Zipf, L.: PARASO, a circum-Antarctic fully-coupled ice-sheet - ocean - sea-ice - atmosphere - land
894 model involving f.ETISH1.7, NEMO3.6, LIM3.6, COSMO5.0 and CLM4.5 *Geosci. Model Dev.* 15, 553–
895 594, <https://doi.org/10.5194/gmd-15-553-2022>, 2022a.



- 896 Pelletier C., Fichefet, T., Goosse, H., Haubner, K., Helsen, S., Huot, P.-V., Kittel, C., Klein, F., Le
897 clec'h, S., van Lipzig, N. P. M., Marchi, S., Massonnet, F., Mathiot, P., Moravveji, E., Moreno, E.,
898 Ortega, P., Pattyn, F., Souverijns, N., Van Achter, G., Vanden Broucke, S., Vanhulle, A., Verfaillie, D.,
899 and Zipf, L.: Corrigendum to 'PARASO, a circum-Antarctic fully-coupled ice-sheet - ocean - sea-ice -
900 atmosphere - land model involving f.ETISH1.7, NEMO3.6, LIM3.6, COSMO5.0 and CLM4.5' Corr. to
901 Geosci. Model Dev. 15, 553–594, <https://doi.org/10.5194/gmd-15-553-2022-corrigendum>; 2022b.
902 Raphael, M. N., Handcock, M. S., Holland, M. M. and Landrum, L. L.: An assessment of the
903 temporal variability in the annual cycle of daily Antarctic sea ice in the NCAR Community Earth
904 System Model, Version 2: A comparison of the historical runs with observations, J. Geophys. Res.:
905 Oceans 125, e2020JC01645, <https://doi.org/10.1029/2020JC016459>, 2020.
906 Roach, L. A., Horvat, C., Dean, S. M., and Bitz, C. M.: An emergent sea ice floe size distribution in
907 a global coupled ocean-sea ice model, J. Geophys. Res.: Oceans, 123, 4322–4337,
908 <https://doi.org/10.1029/2017JC013692>, 2018.
909 Roach, L. A., Bitz, C. M., Horvat, C., and Dean, S. M.: Advances in modeling interactions between
910 sea ice and ocean surface waves. J. Adv. Mod. Earth Sys. 11, 4167–4181,
911 <https://doi.org/10.1029/2019MS001836>, 2019.
912 Roach, L. A., Dörr, J., Holmes, C. R., Massonnet, F., Blockley, E. W., Notz, D., Rackow, T., Raphael,
913 M. N., O'Farrell, S. P., Bailey, D. A., Bitz, C. M.: Antarctic sea ice area in CMIP6, Geophys. Res. Lett., 47,
914 e2019GL086729, <https://doi.org/10.1029/2019GL086729>, 2020.
915 Roach, L. A., Eisenman, I., Wagner, T. J. W., Blanchard-Wrigglesworth, E., Bitz, C. M.: Asymmetry
916 in the seasonal cycle of Antarctic sea ice due to Insolation. Nat. Geosci. 15, 277–281,
917 <https://doi.org/10.1038/s41561-022-00913-6>, 2022.
918 Rockel, B., Will, A., and Hense, A.: The regional climate model COSMO-CLM (CCLM), Meteorol.
919 Z., 17, 347–348, <https://doi.org/10.1127/0941-2948/2008/0309>, 2008.
920 Rousset, C., Vancoppenolle, M., Madec, G., Fichefet, T., Flavoni, S., Barthélemy, A., Benschila, R.,
921 Chanut, J., Levy, C., Masson, S., and Vivier, F.: The Louvain-La-Neuve sea ice model LIM3.6: global and
922 regional capabilities, Geosci. Model Dev., 8, 2991–3005, <https://doi.org/10.5194/gmd-8-2991-2015>,
923 2015.
924 Schroeter, S., and Sandery, P. A.: Large-ensemble analysis of Antarctic sea ice model sensitivity to
925 parameter uncertainty, Ocean Modelling 177, 102090,
926 <https://doi.org/10.1016/j.ocemod.2022.102090>, 2022.
927 Souverijns, N., Gossart, A., Gorodetskaia, I. V., Lhermitte, S., Mangold, A., Laffineur, Q., Delcloo,
928 A., and van Lipzig, N. P. M.: How does the ice sheet surface mass balance relate to snowfall? Insights
929 from a ground-based precipitation radar in East Antarctica, The Cryosphere, 12, 1987–2003,
930 <https://doi.org/10.5194/tc-12-1987-2018>, 2018.
931 Stammerjohn, S. E., Martinson, D. G., Smith, R. C., Yuan, X., and Rind, D.: Trends in Antarctic
932 annual sea ice retreat and advance and their relation to El Niño–Southern Oscillation and Southern
933 Annular Mode variability. J Geophys Res 113:1–20. <https://doi.org/10.1029/2007JC004269>, 2008.
934 Stewart, K., Kim, M., Urakawa, S., McC. Hogg, A., Yeager, S., Tsujino, H., Nakano, H., Kiss, A. E.,
935 Danabasoglu, G.: JRA55-do-based repeat year forcing datasets for driving ocean–sea-ice models,
936 Ocean Model. 147, 101557, <https://doi.org/10.1016/j.ocemod.2019.101557>, 2020.
937 Urrego-Blanco, J. R., Urban, N. M., Hunke, E. C., Turner, A. K., and Jeffery, N.: Uncertainty
938 quantification and global sensitivity analysis of the Los Alamos sea ice model, J. Geophys. Res. Oceans
939 121, 2709–2732, doi:10.1002/2015JC011558, 2016.
940 Vancoppenolle, M., Fichefet, T., Goosse, H., Bouillon, S., Madec, G., and Maqueda, M. A. M.:
941 Simulating the mass balance and salinity of Arctic and Antarctic sea ice. 1. Model description and
942 validation, Ocean Model., 27, 33–53, <https://doi.org/10.1016/j.ocemod.2008.10.005>, 2009.



- 943 Vancoppenolle, M., Bouillon, S., Fichefet, T., Goosse, H. Lecomte, O., Morales Maqueda, M. A.,
944 and Madec, G.: LIM The Louvain-la-Neuve sea Ice Model, Tech. Rep. 31, Note du Pôle de
945 Modélisation de l'Institut Pierre-Simon Laplace No. 31, ISSN No 1288-1619, available at:
946 https://cmc.ipsl.fr/images/publications/scientific_notes/lim3_book.pdf (last access 21 July 2022),
947 2012.
- 948 Verfaillie, D., Pelletier, C., Goosse, H., Jourdain, N.C., Bull, C.Y.S., Dalaiden, Q., Favier, V.,
949 Fichefet, T., and Wille, J. : How does the Southern Annular Mode impact ice-shelf basal melt in
950 Antarctica? *Comm. Earth Envi.* 3, 139, <https://doi.org/10.1038/s43247-022-00458-x>, 2022.
- 951 Watkins, A. B., and Simmonds, I.: A late spring surge in the open water of the Antarctic sea ice
952 pack, *Geophys. Res. Lett.*, 26, 1481–1484. <https://doi.org/10.1029/1999GL900292>, 1999
- 953 Wilson, E.A., Riser, S. C., Campbell, E. C., and Wong, A. P.: Winter upper ocean stability and ice-
954 ocean feedbacks in the sea-ice-covered Southern Ocean. *Journal of Physical Oceanography*, 49,
955 1099–1117, 2019.
- 956 Zuo, H., Balmaseda, M. A., Tietsche, S., Mogensen, K., and Mayer, M: The ECMWF operational
957 ensemble reanalysis–analysis system for ocean and sea ice: a description of the system and
958 assessment, *Ocean Sci.* 15, 779–808, <https://doi.org/10.5194/os-15-779-2019>, 2019.
959